

AD-A065 155

ENVIRONMENTAL RESEARCH AND TECHNOLOGY INC CONCORD MASS

F/G 4/1

MICROWAVE-INFRARED RETRIEVALS.(U)

APR 78 H K BURKE, R K CRANE, M G FOWLER

F19628-76-C-0135

UNCLASSIFIED

AF6L-TR-79-0019

NL

| OF |
AD
A065155
155



LEVEL IV

12

AFGL-TR-79-0019

MICROWAVE-INFRARED RETRIEVALS

H. K. Burke
R. K. Crane
M. G. Fowler
R. D. Rosen

Environmental Research & Technology, Inc.
695 Virginia Road
Concord, Massachusetts 01742

Final Report
1 November 1975 - 30 April 1977

April 1978

DDC
FORM 1
1975

Approved for public release; distribution unlimited

ADA065155

DDC FILE COPY

Environmental Research & Technology, Inc.
695 Virginia Road
Concord, Massachusetts 01742

75 03 28 133

Qualified requesters may obtain additional copies from the Defense Documentation Center. All others should apply to the National Technical Information Service.

Unclassified

SECURITY CLASSIFICATION OF THIS PAGE (When Data Entered)

REPORT DOCUMENTATION PAGE		READ INSTRUCTIONS BEFORE COMPLETING FORM	
1. REPORT NUMBER AFGL-TR-79-0019	2. GOVT ACCESSION NO.	3. RECIPIENT'S CATALOG NUMBER	
4. TITLE (and Subtitle) MICROWAVE-INFRARED RETRIEVALS.	5. TYPE OF REPORT & PERIOD COVERED Final Report Nov 75 - 30 Apr 77	6. PERFORMING ORG. REPORT NUMBER	
7. AUTHOR(s) H. K. Burke, R. D. Rosen R. K. Crane M. G. Fowler	8. CONTRACT OR GRANT NUMBER(s) F19628-76-C-0135	9. PROGRAM ELEMENT, PROJECT, TASK AREA & WORK UNIT NUMBERS 62101F 669804AA	10. REPORT DATE Apr 78
11. CONTROLLING OFFICE NAME AND ADDRESS Air Force Geophysics Laboratory Hanscom AFB, Massachusetts 01731 Monitor/V. J. Falcone/LYS	12. NUMBER OF PAGES 70	13. SECURITY CLASS. (of this report) Unclassified	14. DECLASSIFICATION/DOWNGRADING SCHEDULE
15. DISTRIBUTION STATEMENT (of this Report) Approved for public release; distribution unlimited.			
16. DISTRIBUTION STATEMENT (of the abstract entered in Block 20, if different from Report)			
17. SUPPLEMENTARY NOTES			
18. KEY WORDS (Continue on reverse side if necessary and identify by block number) Radiative transfer Infrared radiometry Multiple scattering Simulation of cloud effects Microwave radiometry			
19. ABSTRACT (Continue on reverse side if necessary and identify by block number) A fast efficient solution to the plane-parallel scattering atmosphere radiative transfer problem was developed for use in simulating the effects of clouds and rain on infrared and microwave passive remote sensing systems. The solution was based upon the use of a variational-iterative procedure. Application of the variational-iterative procedure to simulating the effects of low stratus and thin cirrus clouds revealed that for the window channel (channel 7) of the DMSP infrared sensor system, multiple scattering			

DD FORM 1 JAN 73 1473

EDITION OF 1 NOV 65 IS OBSOLETE

Unclassified

SECURITY CLASSIFICATION OF THIS PAGE (When Data Entered)
391 776 79 02 26 132

Unclassified

SECURITY CLASSIFICATION OF THIS PAGE(When Data Entered)

computations are required to adequately estimate the radiance for both types of clouds. In addition, multiple scattering calculations are required to properly estimate the radiance values for channels 5 and 6 for thin cirrus clouds.

Unclassified

SECURITY CLASSIFICATION OF THIS PAGE(When Data Entered)

TABLE OF CONTENTS

	Page
ABSTRACT	1
1. INTRODUCTION	6
1.1 Objectives	6
1.2 Summary of Results	7
2. BACKGROUND	11
2.1 Required Retrieval Accuracy	11
2.2 Clear Sky Retrievals	13
2.3 Cloud Effects	15
3. A SOLUTION TO THE RADIATIVE TRANSFER EQUATION WITH SCATTERING	19
3.1 Variational-Iterative Method	19
3.2 Extension to Anisotropic Scattering	25
3.3 Results of Model Calculations	29
4. INFRARED RADIANCE SIMULATIONS WITH CLOUDS	57
4.1 Software Modification	57
4.2 Cloud Simulations	57
5. PARTIAL CLOUDINESS IN THE FIELD-OF-VIEW	67
6. CONCLUSIONS	69
REFERENCES	70

ACCESSION No. _____ Date _____

Section ☒ ☐ ☐

DISTRIBUTION/AVAILABILITY CODES

SPECIAL

A

LIST OF ILLUSTRATIONS

Figures		Page
1A	Source Function Profile	37
1B	Mean Intensity (\bar{I}) and Diffused Flux (F) Derived from Source Function in Figure 1A	38
2A	Source Function Profile	39
2B	Mean Intensity (\bar{I}) and Diffused Flux (F) Derived from Source Function in Figure 2A	40
3	Brightness Temperatures and Radiances for Cloud Type A at All Eight IR Channels	60
4	Brightness Temperatures and Radiances for Cloud Type B at All Eight IR Channels	61
5	Brightness Temperatures and Radiances for Cloud Type C at All Eight IR Channels	62
6	Brightness Temperatures and Radiances for Cloud Type D at All Eight IR Channels	63
7	Brightness Temperatures and Radiances for Cloud Type E at All Eight IR Channels	64
8	Brightness Temperatures and Radiances for Cloud Type F at All Eight IR Channels	65

LIST OF TABLES

Tables		Page
1	RMS Retrieval Errors - Midlatitude Spring Profiles	9
2	A Comparison Between Exact and Calculated Values of the Source Functions at the Top and Bottom of the Atmosphere	31
3	Comparison Between Exact and Calculated Values of Intensities at the Top and Bottom of the Atmosphere at Different Angles μ	32
4	Cases of Anisotropic Scattering with Phase Function	34
5	Cases of Anisotropic Scattering with Phase Function	35
6	Cases of Anisotropic Scattering with Phase Function	36
7	Accuracy of the VI Technique	43
8	Accuracy of the VI Technique	44
9	One Layer Tropical Cloud	46
10	Five Layer Tropical Cloud I	47
11	Five Layer Tropical Cloud II	48
12	Summary of Atmospheric Conditions	50
13	Optical Properties for Cirrus Cloud Layers at Different Thicknesses at Different Wavelengths	52
14	Reflection (r) and Transmission (t) through Different Cirrus Cloud Layers at $\lambda = 0.7 \mu$	53
15	Reflection (r) and Transmission (t) through Different Cirrus Cloud Layers at $\lambda = 3 \mu$	54
16	Reflection (r) and Transmission (t) through Different Cirrus Cloud Layers at $\lambda = 10 \mu$	55
17	Summary of Cloud Models and Their Optical Properties at $12 \mu\text{m}$	58

1. INTRODUCTION

1.1 Objectives

The objective of this contract is to provide an optimum procedure for the retrieval of atmospheric temperature profiles from satellite infrared and microwave radiometer data in the presence of clouds. Toward this end, a fast and efficient solution to the radiative transfer equation was developed for the rapid simulation of cloud effects.

The work under this contract was organized into a series of tasks some of which were specified in the original contract (1 November 1975 to 30 June 1976) and the remainder in the modified contract (1 July 1976 to 30 April 1977). Specifically, the tasks were:

Initial Contract -

- Determine an optimum combination of microwave and infrared data to infer atmospheric temperature profiles using the Environmental Research & Technology (ERT) originated microwave-infrared sounder procedure.
- Evaluate the utility of the variational-iterative (VI) algorithm for the operational determination of the environmental parameters of clouds and precipitation.
- Process and analyze Skylab digital data and photography to determine techniques for using near-infrared data to discriminate between clouds and snow cover.

Modified Contract -

- Perform simulation analysis and use the ERT statistical inversion algorithm to evaluate errors in inversion results.
- Investigate methods to optimize inversion results for a cloudy atmosphere.
- Modify and extend the V-I technique to simulate radiative transfer in a cloudy atmosphere.

- Develop a geometrical model for partial beam filling.
- Develop cloud distributions to be used with the geometrical model.

These tasks fall into two categories: the search for an optimum method for the inversion of infrared and microwave data in the presence of clouds, and the processing of Skylab data. Work on the latter task category consisted of computer processing of digital data from three Skylab-4 passes and the preparation of supporting photographic data. The required data were delivered in March 1976 and used by AFGL for further analysis (Bunting, et al, 1977). Work on the former task category will be considered in this report; work on the latter will not be considered further.

1.2 Summary of Results

Under a previous contract, Environmental Research & Technology (ERT) prepared a set of computer programs for the Air Force Geophysics Laboratory (AFGL) to simulate infrared radiances and microwave brightness temperatures and to invert the simulated radiometer measurements to estimate atmospheric temperature profiles (Weichel, 1976). Two inversion procedures were provided, the Statistical Method of Parameter Estimation (as developed by ERT) and the Minimum Information Method (provided by the Air Force Global Weather Central). The microwave brightness temperature simulation programs were developed by ERT and contained facilities for including the effects of precipitation and clouds. The infrared radiance simulation programs as provided by the Air Force Global Weather Central (AFGWC) did not have facilities for the inclusion of cloud effects. Under this contract, the infrared simulation package was modified to simulate cloud effects using the variational-iterative technique for the solution of the radiative transfer equation for a scattering medium.

The variational-iterative (VI) method for the solution of the radiative transfer equation for a plane-parallel scattering atmosphere with azimuthal symmetry was developed by Sze (1976) for the special case of isotropic scattering. This program was modified to include a higher order approximation to the phase function (anisotropic scattering) and

adapted for use in the infrared radiance simulation package operating on the CDC-6600 computer at AFGL.

The infrared simulation package was also updated to calculate radiances for all the DMSP infrared sounder channels. At the same time, the program was updated to conform to the latest (early 1976) operational version of the AFGWC retrieval software. In the process of working with retrievals using the updated Minimum Information Method as used by AFGWC, rather large retrieval errors were discovered. The sources of the discrepancies were investigated. In this process, a number of errors and shortcomings in the numerical solutions and programming logic of the AFGWC programs were discovered. AFGWC was advised of these problems by the contract monitor.

The corrected infrared simulation package (not including the modifications to include cloud effects) and the microwave simulation package were used to statistically investigate infrared, microwave, and infrared plus microwave retrievals of temperature profiles for clear sky conditions and microwave retrievals for cloudy conditions. Clouds generally have a catastrophic effect on temperature retrievals obtained using infrared radiances. In most retrieval methods, cloud contamination is detected early in the process and contaminated data are not used for retrieval. Infrared simulations including cloud effects were made with the modified program only for conditions that might not be detected by the cloud screening algorithms, cases involving thin cirrus clouds and low level stratus clouds.

The retrieval methods were compared using simulated radiance and brightness temperature values calculated using an ensemble of midlatitude (Washington, D.C.) spring radiosonde profiles. Inversions were obtained for clear and cloudy (microwave only) conditions with and without additive instrument (measurement) noise using the Statistical Method for Parameter Estimation (SMPE) and, for infrared only, the Minimum Information Method (MIM). The results are shown in Table 1. The root mean square (rms) differences (errors) give a measure of the difference between the actual and estimated temperature at 5 pressure levels. The results show that for clear sky conditions, the microwave only and the infrared only SMPE retrievals yield identical results. The Infrared plus Microwave SMPE retrievals are not significantly better. Under cloudy

TABLE 1
RMS Retrieval Errors - Midlatitude Spring Profiles

Data	Cloud Conditions	Additive Noise (rms)	Retrieval Method	RMS Differences (error)				
				Surface (°K)	850 mb (°K)	700 mb (°K)	500 mb (°K)	400 mb (°K)
Infrared	clear	none	SMPE*	3.0	2.0	1.8	1.2	1.1
Infrared	clear	0.25 erg	SMPE	3.4	2.7	2.0	1.8	1.7
Microwave	clear	none	SMPE	3.2	2.4	2.0	2.1	1.7
Microwave	clear	0.3°K	SMPE	3.5	2.6	2.0	2.0	1.5
Microwave	clear	1.0°K	SMPE	5.2	4.0	3.0	2.3	1.7
Infrared & Microwave	clear	none	SMPE	2.8	1.8	1.6	1.2	1.1
Infrared & Microwave	clear	0.25 erg + 0.3°K	SMPE	3.0	2.3	2.2	1.7	1.3
Microwave	cloudy	none	SMPE	3.5	2.5	2.0	2.0	1.7
Microwave	cloudy	1.0°K	SMPE	5.2	3.8	3.0	2.3	1.9
Infrared	clear	3°K 1°T guess + .25 erg	MIM	2.7	2.0	2.3	2.2	2.0
Apriori	-	-	-	9.6	9.3	8.2	7.0	6.3

*SMPE = Statistical Method for Parameter Estimation

MIM = Minimum Information Method (AFGWC)

conditions, the microwave retrievals were not significantly different. These results show that microwave measurements are superior to the infrared measurements for situations where the inherently larger field of view of the microwave antenna does not significantly effect the measurements. Finally, no significant difference was obtained between the MIM and SMPE retrievals although MIM appeared to do slightly better at the surface and poorer at 400 mb.

2. BACKGROUND

2.1 Required Retrieval Accuracy

Infrared radiance measurements have been available from meteorological satellites for a number of years. DMSP satellites have been routinely providing AFGWC with data for operational estimation of temperature profiles. The National Weather Service (NWS) also routinely obtains satellite soundings from the National Oceanic and Atmospheric Administration (NOAA) satellites. In the case of the National Weather Service, the satellite derived temperature soundings obtained near synoptic update time (within several hours of 0000 and 1200 UT) are used to provide input to their numerical weather forecasting model for data sparse regions over the oceans (regions without adequate radiosonde data). Recent analysis of the utility of satellite data by the NWS suggests that their forecast model works as well without satellite data as with satellite data (Tracton and McPherson, 1977). They found that they had sufficient data for ocean areas to adequately update the forecast model and satellite data are not required.

At the present time, most computer forecast models, the users of satellite data, expect the data to be similar in information content to radiosonde data. The satellite is viewed as replacing the radiosonde in regions where radiosonde data are not acquired. The wind information provided by the radiosonde is sought from observations of cloud motion; the temperature and humidity data from infrared radiance or microwave brightness temperature measurements. With the expectation that satellite data are to replace radiosonde data, the yardstick for comparison and error analysis is the radiosonde. Unfortunately, the satellite observations do not have the information content of radiosonde measurements. Data are obtained from a limited number of infrared and/or microwave radiometer channels and the radiometer data are often redundant. The radiosonde measurements on the other hand, are essentially independent at different heights; data at each reported pressure level provides new information. The satellite data cannot compete in terms of information content.

Temperature profiles derived from satellite data retrievals appear to be quite similar to the radiosonde observations. The rms differences

reported in Table 1 are between 2 and 5°K (less than 2 percent). The success of the temperature retrievals is derived not from the adequacy of the radiometers but from the regularity of the atmosphere. The statistical method for parameter inversion utilizes a large number of atmospheric profile measurements and effectively selects (calculates in a least squares sense) the profile that most likely would produce the measured radiances (or brightness temperatures). The Minimum Information Method constructs the profile that produces the smallest perturbation to the first guess profile required to match simulated radiances calculated using the perturbed temperature profile to the measured radiances. In either case, additional information about the state of the atmosphere - either the forecast or the most likely state - is used to obtain a retrieval.

The numerical forecast models also produce temperature profile estimates based upon prior measurements and simplified equations of fluid dynamics. The current state of the art in numerical forecasting is a temperature profile with smaller errors (differences) than those reported in Table 1 (Smagorinsky, 1969). At any synoptic time, the forecast temperature profile has smaller rms errors than the satellite retrievals. The forecast errors are, however, correlated and a forecast model with no temperature profile measurement input will slowly depart from the actual state of the atmosphere, the rate of departure depending upon the particular model.

At the present time, with no massive restructuring of the numerical forecast models and their objective analysis schemes, satellite data are not competitive with radiosonde data or with forecast data in limited data sparse regions over limited time intervals. As a part of the First Global GARP Experiment (FGGE), estimates have been prepared for the maximum temperature errors allowable for use in numerical forecasting. The estimated maximum error is 1° rms (Bengtsson, 1975), a value not currently achievable using satellite data even in the absence of cloud contamination. Satellite data may still be of importance for military application for instances in which no radiosonde data are available. In this case, the satellite data may provide the only connection between the forecast model and reality. Unfortunately, through the strong correlation between the first guess profile and the retrieved values, the forecast model may still rapidly depart from reality when MIM is used to provide the

retrieval. High spatial resolution satellite data may also be useful in the study of the spatial variation of integrated properties of the atmosphere such as total precipitable water. This aspect of the utility of satellite data is not considered in this report.

Modified objective analysis schemes may, in the end, be required before satellite data are useful for input to numerical models. Although many possible atmospheric profiles may produce the observed radiance values, a much smaller number of profiles are consistent both with the spatially developing meteorological fields and with the observed horizontal variation in radiance. The further reduction of the number of possible profiles will reduce the rms differences between estimated and actual temperature values. With a statistical parameter estimation procedure operating on entire radiance maps and forecast fields, the resultant temperature estimation error may drop below the value (or any value) suggested as a prerequisite for the use of satellite data. With the continued development of statistical data assimilation techniques for objective analysis (Bengtsson, 1975), opportunities may arise for improving the performance of temperature data retrieval schemes utilizing satellite measurements.

2.2 Clear Sky Retrievals

The programs required to provide clear sky retrievals using simulated data were provided to AFGL by ERT under a previous contract. The simulation routines and retrieval methods are described by Weichel (1976). The infrared simulation routine was modified and updated under this contract to conform with the latest version (early 1976) of the same routine used operationally in the MIM retrieval package at AFGWC. The program was also used, at the request of the contract monitor, to obtain retrievals from a set of DMSP measurements rather than from simulated radiance values. In the course of trying to match the observed and retrieved temperature values, it was discovered that better results could be obtained by slightly modifying the transmittance values. These results suggest that the filter characteristics used to prepare the transmittance values for the simulation package may be in error.

The results obtained from the infrared simulation package are for a hypothetical infrared radiometer system that has the filter character-

istics used to generate the transmittances for simulation. To the extent that the simulation package represents an approximation to the complex infrared absorption and scattering processes that occur in the atmosphere, the simulation results are for the hypothetical system and atmosphere. Difficulties with the simulation of radiances obtained using NOAA satellites has caused the National Environmental Satellite Service (NESS) to abandon the MIM approach to retrieval, which requires a simulation of the atmosphere and instrument response, in favor of the SMPE approach using measured, not simulated, radiances to construct the D matrix (see Weichel, 1976 for a definition of terms; see Smith and Woolf, 1976 for a discussion of the NESS retrieval system for Nimbus-6)

An investigation of the errors that result from using the SPME retrieval technique and combinations of infrared and microwave measurements was made to determine whether the microwave plus infrared measurements provide more information than either data type alone. A midlatitude spring data set was used for the simulations and temperature profile retrievals. Radiosonde data for March, April, and May for the years 1958 through 1962 were used for the analysis. A detailed discussion of the data set and the method used to extend the data set to reach to a 10 mb pressure level is given in Weichel (1976).

The simulations were made for an over water or ocean situation. The ocean surface was assumed to be a black body at infrared frequencies (emissivity equal to 1.). At microwave frequencies, a more complex ocean surface model was used that included both salinity and sea surface roughness effects (Gaut, et al, 1972). For both data sets, the sea surface temperature was assumed to have a random variation about the surface (1000 mb) level temperature value. The sea surface temperature deviation was normally distributed with a 1.5°K standard deviation. For the microwave simulations the wind speed was assumed to have a 3.8 m/s mean value and a 2.1 m/s standard deviation. The salinity was assumed fixed at 0.66 moles/liter.

The results of the simulations with and without additive radiometer measurement noise are listed in Table 1. The infrared radiometer data included observations (simulated) from 8 channels. The microwave sounder included observations (simulated) from 7 channels. The frequencies and weighting functions for each channel are specified in Weichel

(1976). The channel characteristics are for the DMSP infrared sounder SSE sensor package plus the microwave sounder package to be used on future DMSP satellites. The results are nearly identical to those expected for the SSH package when the 535.35 cm^{-1} F channel is included with the E channels.

For comparison, Smith and Woolf (1976) reported a similar study for the 17 channel High-resolution Infra-Red Sounder (HIRS) and 5 channel SCanning Microwave Spectrometer (SCAMS) on the Nimbus-6 satellite. For clear sky conditions, they obtained results similar to those presented in Table 1, simulated errors between 1° and 2°K at altitudes above 800 mb for 7 infrared channels near $15 \mu\text{m}$ and for the 5 microwave channels plus the same 7 infrared channels. They did not analyze microwave only data. Their results however differ from ours near the surface where their inversion errors are all less than 0.5°K . They were not explicit about the method used to simulate surface temperature or on the role played by surface temperature in the inversion process. At one point they comment that surface temperature may be treated as a known providing an extra channel of information. They therefore may have artificially constrained the surface temperature values.

In summary, for the DMSP satellites and for Nimbus-6, the cloud-free retrieval errors are of the order of 2°K except at the surface. Smith and Woolf found little difference between using infrared alone and using infrared plus microwave data. We find little difference between these two cases and between them and using microwave data alone whether the data are noise-free or simulated as contaminated by a reasonable level of instrument noise.

2.3 Cloud Effects

Clouds may severely affect infrared observations while causing little effect at microwave frequencies. Cloud contamination is a major problem which affects all infrared only inversion schemes. Cloud contamination detection algorithms are used to remove the effects of clouds either by rejecting contaminated data or, in the case of NESS retrievals (Smith and Woolf, 1976) by estimating equivalent cloud-free radiances.

Cloud contamination models have generally been straight forward. At infrared wavelengths, the clouds are assumed to have emissivities near

one and large optical depths. For completely overcast conditions, the clouds provide a lower "surface" and observations may be made down to cloud level. For partly cloudy conditions, the clouds obscure only part of the surface. The radiances from the clouds combine with those from the surface in proportion to their areas. In effect, two radiative transfer problems are solved, one for absorption by the atmosphere above the surface and the other for absorption by the atmosphere above a cloud. Each are handled as plane-parallel problems with a lower surface having unity emissivity (see Crane, 1976 for notation).

$$I_v^s = B_v[T(P_s)]\theta_v(P_s) - \int_0^{P_s} B_v[T(P)] \frac{d\theta_v(P)}{dP} dP \quad (1)$$

$$I_v^c = B_v[T(P_c)]\theta_v(P_c) - \int_0^{P_c} B_v[T(P)] \frac{d\theta_v(P)}{dP} dP \quad (2)$$

where I_v^s is the radiance at the satellite for the lower surface corresponding to the earth's surface, s refers to surface

I_v^c is the radiance at the satellite for the lower surface corresponding to cloud top, c refers to cloud top

$B_v[T(P)]$ is the Planck radiance (see eq. 63)

$T(P)$ is temperature (kinetic)

P is pressure

v is frequency

$\theta(P_s) = e^{-\tau_v} =$ transmittance

τ_v is optical depth = $\int_0^s \gamma_a(y)dy$

$\gamma_a(y)$ is the absorption coefficient at y along the path from 0 to s , from the height of P_s to the satellite.

If N represents the fractional area with clouds within the field of view of the radiometer, then

$$I_v = (1-N)I_v^s + NI_v^c \quad (3)$$

From these equations, it is evident that the radiance values will be lower if clouds appear within the field of view. Cloud contamination may be detected by assuming that adjacent scan positions for a scanning radiometer observe different areas having different amounts of cloudiness but having identical I_v^S radiances. If one scan position has no cloud contamination, it will have the highest radiance value. Using the window channel which primarily measures surface temperature (and water vapor) the effect of clouds will be the largest due to the greatest change of radiance values between viewing the surface and viewing clouds. The cloud detection algorithm that is used by AFGWC assumes that the highest radiance value for a scan area is for the cloud-free location and the cloud-free radiances for the scan area are taken from the assumed cloud-free location. This technique will not detect and correct for cloud contamination if all scan positions view areas with some clouds.

NESS uses the data from adjacent scan spots to compute the fractional area with clouds and, from the computed N values, calculate the equivalent cloud free radiances. This can only be done if two additional pieces of information are known, the radiances in one of the channels for cloud-free conditions and the relative heights of clouds in adjacent scan positions. If the sea surface temperature is known or adequately modeled for the time of the observations, then the radiance value for the window channel may be estimated (using climatological data to account for atmospheric effects such as the additional absorption and emission by water vapor). If, further, the heights of the clouds in adjacent scan positions are assumed to be identical, then the I_v^C values and I_v^S values for adjacent scan spots are known. Using equation (3), the ratios of cloud-free areas for adjacent scan spots can be calculated and from that the equivalent clear sky radiance values. Letting $N^* = N_1/N_2$ the ratio of cloud-free areas (Smith and Woolf, 1976) then

$$I_v^S = \frac{I_{v,1} - N^* I_{v,2}}{1 - N^*} \quad (4)$$

where $I_{v,1}$ and $I_{v,2}$ are the observed radiances for the adjacent scan spots. Equation (4) is used to solve for N^* for the one channel for which I_v^S is known (calculated using the assumed surface temperature and radiative transfer model).

This method or any other for the correction of infrared radiance data using infrared observations alone is subject to a large number of uncertainties. The microwave observations provide a means for removing the uncertainty. Smith and Woolf use the microwave data in their version of the SMPE to estimate N and, in turn, to estimate cloud-free radiances. From the simulation results reported in Table 1, it is evident that microwave data alone will accomplish the same results with little difference in the rms retrieval error. The combined data may however be useful for estimating cloud parameters such as cloud height and fractional cloud area (assuming equation (2)). Both cloud height and fractional area are additional parameters that can be obtained from SMPE inversions of combined infrared and microwave data. At this juncture, an adequate cloud simulation package is required to provide radiance estimates for different cloud height and fractional area values. The required cloud simulation package is considered in the next three sections.

The use of combined infrared and microwave data for temperature and cloud parameter retrievals requires matched observing areas at infrared and microwave frequencies. The microwave systems however inherently observe larger areas due to physical limitations on antenna beamwidths. If the observing areas at infrared and microwave frequencies are identical, then the microwave data alone are adequate for temperature retrieval. If large differences exist between the observing areas then the microwave data are not useful in solving the cloud contamination problem although the microwave data should provide better estimates of I_V^S than estimates from surface temperature models.

3. A SOLUTION TO THE RADIATIVE TRANSFER EQUATION WITH SCATTERING

The inclusion of clouds in the radiative transfer equation complicates the problem due to the addition of scattering by the cloud particles. Instead of the nonlinear quadrature formula represented by equations (1) and (2), the radiative transfer equation becomes an integral equation incorporating the effects of multiple scattering. Numerical solutions to the multiple scattering equations have been available for some time but the procedures have been time consuming and costly to operate. For example, Kattawar and Plass (1969) presented the results of a Monte Carlo simulation of the multiple scattering from water clouds at visible and near infrared wavelengths. Sze (1976) recently developed a rapid method for solving the multiple scattering equation for isotropic scattering in a plane-parallel medium (the scattering properties vary only with height above a plane earth). With the variational-iterative method developed by Sze, computer times are short enough and costs low enough to permit the inclusion of multiple scattering effects in the simulation of infrared radiances. The details of the variational-iterative solution as developed by Sze and extended under this contract to include anisotropic scattering are discussed in this section. The software package provided to AFGL and the results of simulations will be discussed in the next section.

3.1 Variational-Iterative Method

The radiative transfer equation for a plane-parallel scattering atmosphere is given by (Chandrasekhar, 1960):

$$\mu \frac{dI_v(\tau, \mu, \phi)}{d\tau} = I_v(\tau, \mu, \phi) - J_v(\tau, \mu, \phi)$$

where

$$J_v(\tau, \mu, \phi) = \frac{1}{4\pi} \int_{-1}^{+1} \int_0^{2\pi} p(\mu, \phi; \mu^1, \phi^1) I_p(\tau, \mu^1, \phi^1) d\mu^1 d\phi^1$$

$$+ J_o(\tau, \mu, \phi)$$

μ is the cosine of the zenith angle

ϕ is the azimuth angle

J is the source function

J_0 is the primary excitation source function

p is the phase function

and the remaining symbols were defined above. For a scattering plane-parallel atmosphere with the primary source emission from atmospheric gasses or for a plane-parallel atmosphere with an external source (the sun say) and isotropic scattering, the problem has axial symmetry about the zenith direction and the dependence on azimuth can be removed:

$$\mu \frac{dI(\tau, \mu)}{d\tau} = I(\tau, \mu) - J(\tau, \mu) \quad (5)$$

$$J(\tau, \mu) = J_0(\tau, \mu) + \frac{1}{2} \int_{-1}^1 p(\mu, \mu^1) I(\tau, \mu^1) d\mu^1 \quad (6)$$

where the explicit dependence on ν has been suppressed.

The phase function is normalized to represent the total energy scattered by a single scatter relative to the sum of the energy absorbed and scattered by the particle:

$$\frac{1}{4\pi} \int_{-1}^1 \int_0^{2\pi} p(\mu, \phi; \mu^1, \phi^1) d\mu^1 d\phi^1 = \omega_0 \leq 1 \quad (7)$$

where ω_0 is the single scattering albedo. For an isotropic scatterer, $p = \text{constant} = \omega_0$. The primary excitation source function for atmospheric thermal emission is

$$J_0(\tau) = (1 - \omega_0(\tau)) B[T(\tau)] \quad (8)$$

where $B[T(\tau)]$ is B_ν , the Planck function. In this representation of the radiative transfer equation, the distance from the top or bottom of the atmosphere is measured in units of optical depth, τ , rather than distance or pressure. The point properties of the medium such as the single scattering albedo are then functions of τ .

$$\tau(\zeta) = \int_{\zeta}^{\infty} \gamma_e(\zeta) d\zeta \quad (9)$$

$$\omega_o(\zeta) = \frac{\gamma_e(\zeta) - \gamma_a(\zeta)}{\gamma_e(\zeta)} \quad (10)$$

where γ_e is the volume extinction coefficient (cross section per unit volume)

γ_a is the absorption coefficient as defined above and ζ = height.

Equation (5) reduces to (1) above when $\gamma_e = \gamma_a$ or $\omega_o = 0$.

From equations (7), (8) and (9), the source function can be written as

$$\begin{aligned} J(\tau) = & 1 - \omega_o(\tau) B(T(\tau)) + \frac{\omega_o(\tau)}{2} \int_0^{\tau^*} J(\tau) E_1(|\tau - \tau^*|) d\tau \\ & + \frac{\omega_o(\tau)}{2} \int_0^1 I(\tau^*, \mu^1) e^{-(\tau^* - \tau)/\mu^1} d\mu^1 \end{aligned} \quad (11)$$

where E_1 is the exponential integral of the first order and

τ^* is the total optical depth such that $I(\tau^*, \mu)$ is the outgoing (upwelling) intensity at the lower boundary (surface).

The exponential integral E_n of the nth order is defined as

$$E_n(x) = \int_0^1 e^{-x/\mu} \mu^{n-2} d\mu; \quad n = 1, 2, \dots$$

$I(\tau^*, \mu)$ has two contributions: (1) surface emission and (2) surface reflection. For a surface reflectivity, R , and temperature, T_s ,

$$I_1(\tau^*, \mu) = (1 - R) B(T_s) \quad (12)$$

$$I_2(\tau^*, \mu) = 2 \cdot R \cdot \int_0^1 I(\tau^*, -\mu^1) \mu^1 d\mu^1 \quad (13)$$

where $I(\tau^*, -\mu^1)$ is the downward intensity at the surface in the direction corresponding to μ^1 .

Equation (13) is based on the assumption of a Lambertian surface; there will be an "isotropic" reflection independent of the incident angle on the surface. Equation (13) can further be written as

$$I_{(2)}(\tau^*, \mu) = 2 \cdot R \cdot \int_0^{\tau^*} J(t) E_2(\tau^* - t) dt \quad (14)$$

where E_2 is the second order exponential integral. Combining (11), (12) and (13) we obtain the expression for the source function:

$$\begin{aligned} J(\tau) = & (1 - \omega_0(\tau)) B(T(\tau)) + \frac{\omega_0(\tau)}{2} \int_0^{\tau^*} J(t) E_1(|t - \tau|) dt \\ & + \frac{\omega_0(\tau)}{2} \cdot E_2(\tau^* - \tau) [(1 - R) B(T_{gr}) + 2 \cdot R \cdot \int_0^{\tau^*} J(t) E_2(\tau^* - t) dt] \end{aligned} \quad (15)$$

The outgoing intensity at the top of the atmosphere then can be expressed as

$$\begin{aligned} I(0, \mu) = & \int_0^{\tau^*} J(t) e^{-t/\mu} dt / \mu + (1 - R) B(T_{gr}) e^{-\tau^*/\mu} \\ & + 2 \cdot R \cdot \left[\int_0^{\tau^*} J(t) E_2(\tau^* - t) dt \right] e^{-\tau^*/\mu} \end{aligned} \quad (16)$$

The three terms on the right hand side of equation (16) are

- (1) the upward emission from the atmosphere (including clouds),
- (2) the emission of the attenuated background surface, and
- (3) the reflection of the downward atmospheric emission from the surface.

The variational-iterative (VI) approach (Sze, 1976) is used to solve this system of equations. The variational method depends on finding the "extremum" of a certain functional; an a priori form is used for the unknown function and the coefficients are found from a set of minimizing conditions. In essence, this method provides a direct way for constructing an approximate solution for the source function. The atmosphere is divided into subintervals and the source function is approximated as a combination of step functions in different intervals. The advantages of this technique are that: (1) it is fast and requires

little computational time to achieve satisfactory accuracy, and (2) it allows vertical inhomogeneity and the inclusion of surface reflection.

The VI technique provides a direct method for constructing an approximate solution to the integral equation (15) for the source function. An approximate source function can be expressed as

$$J_a(\tau) = U_a(\tau) \sqrt{\omega_0(\tau)} \quad (17)$$

where

$$U_a(\tau) = \sum_{i=1}^N C_i V_i(\tau)$$

and the $V_i(\tau)$ are known trial functions. The choice of trial functions plays an important role in the ultimate success of the variational method (Kourganoff, 1963). In the variational solution employed by Sze, simple step functions were chosen as the trial functions. This choice (1) makes it simple to perform the integrals required in (15) and (2) the intervals can be chosen to resemble multiple cloud layers, the weights $C_i \sqrt{\omega_i}$ for each layer represent the average source function in that layer where ω_i is the single scattering albedo for the layer.

The total optical depth τ^* is divided into $N-1$ intervals with ω_i constant over each interval. The trial function then is

$$V_j(\tau) = \begin{cases} 1 & \tau_j < \tau \leq \tau_{j+1} \\ 0 & \text{otherwise} \end{cases}$$

The C_i then are solutions of the algebraic equation

$$\sum_{j=1}^N M_{ij} C_j = f_i \quad (19)$$

where

$$M_{ij} = \delta_{ij} \Delta\tau_j - \sqrt{\frac{\omega_i \omega_j}{2}} \int_{\tau_i}^{\tau_{i+1}} D_j(\tau) d\tau \quad (20)$$

$$\delta_{ij} = \begin{cases} 0, & i \neq j \\ 1, & i = j \end{cases}$$

$$D_j(\tau) = \int_{\tau}^{\tau_j+1} E_1(|\tau-t|) dt$$

$$\text{and } f_i = \left(\frac{1-\omega_i}{\sqrt{\omega_i}} \right) B(T(\tau_i)) + \frac{\sqrt{\omega_i}}{2} E_2(\tau^*-\tau_i) (1-R) B(T_s) \quad (21)$$

The variational solution is an approximation to the actual solution which is correct at least at one level within each layer (Sze, 1976). A smoothed approximation for the source function then can be constructed:

$$\begin{aligned} J_1(\tau) &= (1-\omega_0(\tau)) B(T(\tau)) + \frac{\omega_0(\tau)}{2} E_2(\tau^*-\tau) (1-R) B(T_s) \\ &+ \frac{\omega_0(\tau)}{2} \sum_{j=1}^{N-1} C_j \sqrt{\omega_j(\tau)} D_j(\tau) \\ &+ \omega_0(\tau) E_2(\tau^*-\tau) R \sum_{j=1}^{N-1} C_j \sqrt{\omega_j(\tau)} \int_{\tau_j}^{\tau_j+1} E_2(\tau^*-t) dt \end{aligned} \quad (22)$$

Since the smoothed approximation is a summation over layers with oscillating residual errors, it provides a reasonable first estimate of the true source function (Burke and Sze, 1977). Improved accuracy may be obtained by further iterations of the integral equation for the source function as:

$$\begin{aligned} J_{n+1}(\tau) &= (1-\omega_0(\tau)) B(T(\tau)) + \frac{\omega_0(\tau)}{2} E_2(\tau^*-\tau) (1-R) B(T_s) \\ &+ \frac{\omega_0(\tau)}{2} \int_0^{\tau^*} E_1(|\tau-t|) J_n(t) dt \\ &+ \omega_0(\tau) E_2(\tau^*-\tau) R \int_0^{\tau^*} E_2(\tau^*-t) J_n(t) dt \end{aligned} \quad (23)$$

The residue of the n th iteration is defined as

$$\Delta_n = \left| \frac{J_n - J_{n-1}}{J_n} \right| \quad (24)$$

By specifying the maximum residue allowed, the iteration process then brings the source function to desired accuracy. The number of iterations for the system also depends on the choice of the number of step functions

in the matrix formalism (the number N , see eq. 17). For example, we consider a fully scattering ($\omega_0 = 1$) medium with $\tau^* = 3.5$. By dividing the medium into two step functions ($N=2$) it takes seven iterations to bring the maximum residue in the source function to less than 1%. However, by representing the medium by four step functions it takes only two iterations to obtain the same accuracy.

3.2 Extension to Anisotropic Scattering

Rain and cloud particles range in size from smaller than a wavelength to many wavelengths at microwave and infrared frequencies. Over this size range, the energy radiated by scattering is not scattered isotropically in all directions but is scattered selectively into forward and backward lobes. The relative intensity of the scattering in any direction is described by the phase function (equation 7). In general, the phase function for randomly oriented scatterers, and for natural or unpolarized thermal emission can be expanded in a series of Legendre polynomials as

$$p(\cos \theta) = \sum_{\ell=0}^{\infty} \omega_{\ell} P_{\ell}(\cos \theta) \quad (25)$$

where P_{ℓ} = Legendre polynomial
 θ = scattering angle.

In addition to the simplest case of isotropic scattering, two phase functions have found extensive use in describing particulate scatter, Rayleigh's phase function

$$p(\cos \theta) = \frac{3\omega_0}{4} (1 + \cos^2 \theta) \quad (26)$$

which may be used when the particles are small compared to a wavelength and

$$p(\cos \theta) = \omega_0 (1 + \chi \cos \theta) \quad (-1 \leq \chi \leq 1) \quad (27)$$

which is often used as a first, 2-term, approximation to equation (25) for problems with particles large relative to a wavelength having significant differences between the forward and backscattered energies. χ is used to adjust the relative magnitude of the forward and backscattered energies. For applications at infrared frequencies, the latter approximation was used to characterize anisotropic scattering.

The two term approximation is often used in the study of radiative transfer in planetary atmospheres because it is easy to handle analytically and provides a good approximation to the integrated effects caused by predominantly forward and backward scattering particles. For radiative transfer problems with azimuthal symmetry or in problems employing azimuthally averaged radiances,

$$\int_0^{2\pi} \cos \theta \, d\phi' = \mu \mu'$$

hence
$$p(\mu, \mu') = \omega_0(1 + \chi\mu\mu') \quad (28)$$

Using this form for the phase function, the source function becomes

$$J(\tau, \mu) = \frac{\omega_0(\tau)}{2} \left[\int_{-1}^1 I(\tau, \mu') d\mu' + \chi(\tau) \mu \int_{-1}^1 I(\tau, \mu') \mu' d\mu' \right] + J_0(\tau, \mu) \quad (29)$$

or
$$J(\tau, \mu) = J_1(\tau) + \mu J_2(\tau) \quad (30)$$

where
$$J_1(\tau) = \frac{\omega_0(\tau)}{2} \int_{-1}^1 I(\tau, \mu') d\mu' + J_{01}(\tau) \quad (31)$$

and
$$J_2(\tau) = \frac{\omega_0(\tau)}{2} \chi(\tau) \int_{-1}^1 I(\tau, \mu') \mu' d\mu' + J_{02}(\tau) \quad (32)$$

Employing the formal solutions of (5) for $I(\tau, \mu)$ and $I(\tau, -\mu)$, the outgoing and inward intensities,

$$\begin{aligned} I(\tau, \mu) &= \int_{\tau}^{\tau^*} J(t, \mu) \exp(-(t-\tau)/\mu) \, dt/\mu \\ &= \int_{\tau}^{\tau^*} (J_1(t) + \mu J_2(t)) \exp(-(t-\tau)/\mu) \, dt/\mu \end{aligned}$$

and

$$\begin{aligned} I(\tau, -\mu) &= \int_0^{\tau} J(t, -\mu) \exp(-(\tau-t)/\mu) \, dt/\mu \\ &= \int_0^{\tau} (J_1(t) - \mu J_2(t)) \exp(-(\tau-t)/\mu) \, dt/\mu \end{aligned}$$

Proceeding in a manner similar to the development in section 3.1, the boundary conditions for the surface are incorporated to produce a coupled set of integral equations for $J_1(\tau)$ and $J_2(\tau)$:

$$J_1(\tau) = \frac{\omega_0(\tau)}{2} \int_0^{\tau^*} [E_1(|\tau-t|) J_1(t) + E_2(|\tau-t|) b(t-\tau) J_2(t)] dt \quad (33)$$

$$+ (1-\omega_0(\tau))B(T(\tau)) + \frac{\omega_0(\tau)}{2} (1-R) B(T_S) E_2(\tau^*-\tau)$$

$$+ \omega_0(\tau) R E_2(\tau^*-\tau) \int_0^{\tau^*} [E_2(\tau^*-t) J_1(t) - E_3(\tau^*-t) J_2(t)] dt$$

$$\text{and } J_2(\tau) = \frac{\omega_0(\tau)}{2} \chi(\tau) \int_0^{\tau^*} [E_2(|\tau-t|) b(t-\tau) J_1(t) + E_3(|\tau-t|) J_2(t)] dt \quad (34)$$

$$+ \frac{\omega_0(\tau)}{2} \chi(\tau) (1-R) B(T_S) E_3(\tau^*-\tau)$$

$$+ \omega_0(\tau) \chi(\tau) R E_3(\tau^*-\tau) \int_0^{\tau^*} [E_2(\tau^*-t) J_1(t) - E_3(\tau^*-t) J_2(t)] dt$$

where the function $b(x)$ is defined as

$$b(x) = \begin{cases} -1, & x < 0 \\ 1, & x > 0 \end{cases}$$

In matrix notation, (33) and (34) can be expressed as

$$\begin{pmatrix} J_1(\tau) \\ J_2(\tau) \end{pmatrix} = \frac{\omega_0(\tau)}{2} \int_0^{\tau^*} \begin{bmatrix} E_1(|\tau-t|) & E_2(|\tau-t|) b(t-\tau) \\ \chi(\tau) E_2(|\tau-t|) b(t-\tau) & \chi(\tau) E_3(|\tau-t|) \end{bmatrix} \begin{pmatrix} J_1(t) \\ J_2(t) \end{pmatrix} dt$$

$$+ \begin{pmatrix} 1-\omega_0(\tau) \\ 0 \end{pmatrix} B(T_S) + \frac{\omega_0(\tau)}{2} (1-R) \begin{pmatrix} E_2(\tau^*-\tau) \\ \chi(\tau) E_3(\tau^*-\tau) \end{pmatrix} B(T_S) \quad (35)$$

$$+ \omega_0(\tau) \cdot R \begin{pmatrix} E_2(\tau^*-\tau) \\ \chi(\tau) E_3(\tau^*-\tau) \end{pmatrix} \int_0^{\tau^*} [E_2(\tau^*-t) J_1(t) - E_3(\tau^*-t) J_2(t)] dt$$

The variational-iterative technique is used to obtain a solution to the coupled integral equation set (35).

A similar set of linear algebraic equations can be written:

$$\sum_{j=1}^{2n} M_{ij} C_j = f_i \quad (36)$$

The size of the matrix M is $2n \times 2n$ where n is the number of steps. The matrix can be divided into quadrants, $M1$, $M2$, $M3$ and $M4$ such that

$$M1_{ij} = M_{ij}$$

$$M2_{ij} = M_{i,n+j}$$

$$M3_{ij} = M_{n+1,j}$$

$$M4_{i,j} = M_{n+i,n+j}$$

where $i=1, 2, \dots, n$, $j=1, 2, \dots, n$, and

$$M1_{i,j} = \delta_{ij}(\Delta\tau_j) - \frac{\omega_0(\tau_i)}{2} \int_{\tau_i}^{\tau_i+1} \int_{\tau_j}^{\tau_j+1} E_1(|\tau-t|) dt d\tau \quad (37)$$

$$M2_{i,j} = - \frac{\omega_0(\tau_i)}{2} \int_{\tau_i}^{\tau_i+1} \int_{\tau_j}^{\tau_j+1} E_2(|\tau-t|) b(t-\tau) dt d\tau \quad (38)$$

$$M3_{i,j} = - \frac{\omega_0(\tau_i)}{2} \chi(\tau_i) \int_{\tau_i}^{\tau_i+1} \int_{\tau_j}^{\tau_j+1} E_2(|\tau-t|) b(t-\tau) dt d\tau \quad (39)$$

$$M4_{i,j} = \delta_{ij}(\Delta\tau_j) - \frac{\omega_0(\tau_i)}{2} \chi(\tau_i) \int_{\tau_i}^{\tau_i+1} \int_{\tau_j}^{\tau_j+1} E_3(|\tau-t|) dt d\tau \quad (40)$$

with $\delta_{ij} = \begin{cases} 1, & i = j \\ 0, & i \neq j \end{cases}$ $\Delta\tau_i = \tau_{i+1} - \tau_i$

The forcing terms f_i are defined as

$$f_i = \int_{\tau_i}^{\tau_i+1} [(1-\omega_0(\tau))B(T_s) + \frac{\omega_0(\tau)}{2} (1-R)E_2(\tau^*-\tau)B(T_s)] d\tau \quad (41)$$

for $i=1, 2, \dots, n$,

$$\text{and } f_i = \int_{\tau_i}^{\tau_i+1} \frac{\omega_0(\tau)}{2} \chi(\tau) (1-R)E_3(\tau^*-\tau)B(T_s) d\tau \quad (42)$$

for $i=n+1, \dots, 2n$

3.3 Results of Model Calculations

The VI technique was used to prepare results that could be compared with previous calculations. This was done (1) to test the VI technique and the programs developed under this contract and (2) to provide insight into the effects of multiple scattering on atmospheric emission estimates.

3.3.1 Solar Diffusion Results

A considerable literature exists on the solution to the radiative transfer equation where the primary excitation term describes radiant energy from the sun. In this case (see equation (8) for comparison)

$$J_o(\tau, \mu) = \frac{p(\mu, -\mu_o)}{4} \exp(-\tau/\mu_o)$$

where μ_o is the cosine of the incidence angle (zenith) for the solar radiation. For anisotropic scattering an azimuthally averaged intensity may be determined using the axial symmetric formulation (eq. 6) and the phase function approximation introduced in equation (28),

$$J_o(\tau, \mu) = \frac{\omega_o(\tau)}{4} \exp(-\tau/\mu_o) (1 - \chi(\tau)\mu\mu_o) \quad (43)$$

The coupled integral equations then are

$$\begin{pmatrix} J_1(\tau) \\ J_2(\tau) \end{pmatrix} = \frac{\omega_o(\tau)}{2} \int_0^{\tau^*} \begin{bmatrix} E_1(|\tau-t|) & E_2(|\tau-t|)b(t-\tau) \\ \chi E_2(|\tau-t|)b(t-\tau) & \chi E_3(|\tau-t|) \end{bmatrix} \begin{pmatrix} J_1(t) \\ J_2(t) \end{pmatrix} dt \\ + \frac{\omega_o(\tau)}{4} \exp(-\tau/\mu_o) \begin{pmatrix} 1 \\ -\chi(\tau)\mu_o \end{pmatrix} \quad (44)$$

The coupled equations are solved using the VI technique as developed above. Once $J_1(\tau)$ and $J_2(\tau)$ are determined, the azimuth and zenith angle averaged mean intensity ($\bar{I}(\tau)$) and vertical flux ($\pi F(\tau)$) throughout the medium are immediately obtained as

$$\bar{I}(\tau) = 1/2 \int_{-1}^1 I(\tau, \mu) d\mu = \frac{1}{\omega_o(\tau)} [J_1(\tau) - \frac{\omega_o(\tau)}{4} \exp(-\tau/\mu_o)] \quad (45)$$

and

$$F(\tau) = 2 \int_{-1}^1 I(\tau, \mu) \mu d\mu \\ = \frac{4}{\omega_o(\tau)} [J_2(\tau) + \frac{\omega_o(\tau)}{4} \chi(\tau)\mu_o \exp(-\tau/\mu_o)] \quad (46)$$

$X = 0$ represents the special case of isotropic scattering. In this case the source function is reduced to $J(\tau, \mu) = J_1(\tau)$, independent of μ . Therefore, by setting $X = 0$ in solving equation (44), we get solutions for the isotropic system. The results are compared with the exact solutions obtained from Chandrasekhar's X , Y functions (1960) by setting the maximum residue (Δ max %) in the source function to less than 0.02%. The relations of X , Y functions to intensity and source function are:

$$I(o, \mu) = 1/4 \omega_o F \frac{\mu_o}{\mu + \mu_o} [X(\mu) X(\mu_o) - Y(\mu) Y(\mu_o)] \quad (47)$$

$$I(\tau^*, -\mu) = 1/4 \omega_o F \frac{\mu_o}{\mu - \mu_o} [Y(\mu) X(\mu_o) - X(\mu) Y(\mu_o)] \quad (48)$$

$$J(o) = 1/4 \omega_o F X(\mu_o) \quad (49)$$

$$J(\tau^*) = 1/4 \omega_o F Y(\mu_o) \quad (50)$$

The tabulated values of X , Y functions for different ω_o s and τ^* s were taken from Carlstedt and Mullikin (1966).

The cases presented are $\tau^* = 1$, $\mu_o = 1$ for $\omega_o = .5$ and 1. Table 2 is the comparison of the source functions at the top and bottom of the atmosphere. It shows that for $\omega_o = .5$, the calculated values are close to error-free; they agree with the exact values at up to four figures after the decimal point. For the conservative scattering case ($\omega_o = 1$), the error is still within 0.2%

Table 3 shows, under the same atmospheric conditions as in Table 2, the comparison of intensities at the top and bottom of the atmosphere at different angles (μ). The results indicate that for $\omega_o = .5$, the errors in intensities, both outward and inward, are generally less than or in the neighborhood of 0.1%. For $\omega_o = 1$, the error still lies within 0.3%.

From these results, we are convinced that the variational-iterative scheme is a very accurate method in solving radiative transfer problems. This lays an important foundation for the anisotropic cases because "exact" solutions are not available for these cases. We now can control

TABLE 2

A COMPARISON BETWEEN EXACT AND CALCULATED VALUES OF THE
SOURCE FUNCTIONS AT THE TOP AND BOTTOM OF THE ATMOSPHERE
CASES CONSIDERED ARE $\tau^* = 1$, $\mu_o = 1$ for $\omega_o = .5$ and 1

ω_o	J	Exact	Calculated	Error (%)
1	J(o)	0.439345	0.438763	0.13%
	J(τ^*)	0.241511	0.241123	0.16%
.5	J(o)	0.153271	0.153242	0.02%
	J(τ^*)	0.065926	0.065924	0.00%

TABLE 3

COMPARISON BETWEEN EXACT AND CALCULATED VALUES OF INTENSITIES AT THE TOP AND BOTTOM OF THE ATMOSPHERE AT DIFFERENT ANGLES μ . CASES CONSIDERED ARE

$$\tau^* = 1, \mu_0 = 1 \text{ for } \omega_0 = .5 \text{ and } 1$$

ω_0	$I(\tau, \mu)$	Exact	Calculated	Error
1	$I(0, 1)$	0.269393	0.268759	0.23%
	$I(0, 0.8)$	0.30680	0.306064	0.24%
	$I(0, 0.6)$	0.353534	0.352666	0.24%
	$I(0, 0.4)$	0.409034	0.407976	0.26%
	$I(0, 0.2)$	0.458037	0.456708	0.29%
	$I(\tau^*, -0.8)$	0.274833	0.274301	0.19%
	$I(\tau^*, -0.6)$	0.306037	0.305458	0.19%
	$I(\tau^*, -0.4)$	0.332541	0.331954	0.18%
	$I(\tau^*, -0.2)$	0.325061	0.324623	0.13%
0.5	$I(0, 1)$	0.076583	0.076521	0.08%
	$I(0, 0.8)$	0.087701	0.087625	0.09%
	$I(0, 0.6)$	0.101983	0.101888	0.09%
	$I(0, 0.4)$	0.120045	0.119913	0.11%
	$I(0, 0.2)$	0.140087	0.139865	0.16%
	$I(\tau^*, -0.8)$	0.074490	0.074478	0.02%
	$I(\tau^*, -0.6)$	0.082344	0.082339	0.01%
	$I(\tau^*, -0.4)$	0.088386	0.088396	0.01%
	$I(\tau^*, -0.2)$	0.084772	0.084824	0.01%

the desired accuracy by iterating the solution until the residue in the source function is small enough to be acceptable.

A wide range of different atmospheric conditions (both on τ^* and ω_0 and on phase function $p(\mu, \mu') = \omega_0(1 + X\mu\mu')$ were tested. Shown in Tables 4, 5 and 6 is a summary of the representative cases. The optical depths (τ^*) chosen are 0.25, 1 and 4, with single scattering albedos $\omega_0 = 1$ and 0.5. Three x 's, -1, 0.5 and 1, were used. The exact solutions were obtained by the variational method with successive iterations such that the maximum residue in the source function was always less than 0.1%.

The quantities presented are the azimuthally averaged mean intensity (\bar{I}) and vertical flux (F) both at the top and bottom of the atmosphere. The results of the variational technique without iterations and the two-stream method (Liou, 1973) are also included in the tables for the purpose of comparison.

Generally speaking, errors in the variational technique lie within 2% for $\tau^* = .25$, 10% for $\tau^* = 1$ and 20% for $\tau^* = 4$. On the other hand, errors in the two-stream method can get higher than 50% for $\tau^* = .25$, 30% for $\tau^* = 1$ and 20% for $\tau^* = 4$.

From these results, it is obvious that the variational technique is much more accurate than the widely used two-stream method for the anisotropic scattering case considered ($p(\mu, \mu') = \omega_0(1 + x\mu\mu')$). Furthermore, once the algorithm is available, the computational time is also minimal. Therefore, we can conclude that we have developed a far more powerful technique in dealing with first order anisotropic scattering.

Inhomogeneity is an important aspect of the radiative transfer problem. In most approaches, it involves matching boundary conditions for every region of different ω_0 , which could be a tedious job. Inhomogeneity can be directly incorporated in the variational approach through step function approximations without introducing extra computational complexities. For instance, the two-step function is sufficient for handling a two-layer cloud problem. The capability of the variational technique to represent vertical inhomogeneities thus provides a great simplicity in treating cloudy atmospheres.

Figures 1 and 2 provide examples for inhomogeneous atmospheres. Profiles of the source function, mean intensity and diffused flux are presented for the two different cases considered. Both cases deal with

TABLE 4

CASES OF ANISOTROPIC SCATTERING WITH PHASE FUNCTION

$$p(\mu, \mu') = \omega_0(1 + x\mu\mu') \text{ and } \tau^* = .25, \mu_0 = 1.$$

		Exact	Variational $\Delta\%$		2-Stream $\Delta\%$	
$\omega_0 = 1$ $x = 1$	$F^+(0)$	0.6352(-1)	0.6365(-1)	0.2%	0.5538(-1)	12.8%
	$F^+(\tau^*)$	0.1573(0)	0.1576(0)	0.2%	0.1658(0)	5.4%
	$\bar{I}(0)$	0.5561(-1)	0.5587(-1)	0.5%	0.2398(-1)	55.9%
	$\bar{I}(\tau^*)$	0.9573(-1)	0.9625(01)	0.5%	0.7180(-1)	25.0%
$\omega_0 = 1$ $x = .5$	$F^+(0)$	0.8818(-1)	0.8817(-1)	0.0%	0.8426(-1)	4.4%
	$F^+(\tau^*)$	0.1327(0)	0.1330(-1)	0.2%	0.1369(0)	3.2%
	$\bar{I}(0)$	0.6680(-1)	0.6685(-1)	0.1%	0.3648(-1)	45.4%
	$\bar{I}(\tau^*)$	0.8455(-1)	0.8528(-1)	0.9%	0.5930(-1)	29.9%
$\omega_0 = 1$ $x = -1$	$F^+(0)$	0.1549(0)	0.1545(0)	0.3%	0.1612(0)	4.1%
	$F^+(\tau^*)$	0.6602(-1)	0.6674(-1)	1.1%	0.6002(-1)	0.0%
	$\bar{I}(0)$	0.9706(-1)	0.9652(-1)	0.6%	0.6979(-1)	28.1%
	$\bar{I}(\tau^*)$	0.5428(-1)	0.5560(-1)	2.4%	0.2599(-1)	52.1%
$\omega_0 = .5$ $x = 1$	$F^+(0)$	0.2288(-1)	0.2286(-1)	0.1%	0.2293(-1)	0.2%
	$F^+(\tau^*)$	0.6809(-1)	0.6822(-1)	0.2%	0.7603(-1)	11.7%
	$\bar{I}(0)$	0.2179(-1)	0.2172(-1)	0.3%	0.9930(-2)	54.4%
	$\bar{I}(\tau^*)$	0.4068(-1)	0.4093(-1)	0.6%	0.3292(-1)	19.1%
$\omega_0 = .5$ $x = .5$	$F^+(0)$	0.3457(-1)	0.3464(-1)	0.2%	0.3665(-1)	6.0%
	$F^+(\tau^*)$	0.5655(-1)	0.5640(-1)	0.3%	0.6238(-1)	10.3%
	$\bar{I}(0)$	0.2689(-1)	0.2702(-1)	0.5%	0.1587(-1)	41.0%
	$\bar{I}(\tau^*)$	0.3579(-1)	0.3550(-1)	0.8%	0.2701(-1)	24.5%
$\omega_0 = .5$ $x = -1$	$F^+(0)$	0.6810(-1)	0.6791(-1)	0.3%	0.7539(-1)	10.7%
	$F^+(\tau^*)$	0.2315(-1)	0.2337(-1)	1.0%	0.2386(-1)	3.1%
	$\bar{I}(0)$	0.4190(-1)	0.4160(-1)	0.7%	0.3264(-1)	22.1%
	$\bar{I}(\tau^*)$	0.2075(-2)	0.2116(-1)	1.9%	0.1033(-1)	50.2%

TABLE 5

CASES OF ANISOTROPIC SCATTERING WITH PHASE FUNCTION

$$p(\mu, \mu') = \omega_0(1 + x\mu\mu') \text{ and } \tau^* = 1, \mu_0 = 1.$$

		Exact	Variational $\Delta\%$		2-Stream $\Delta\%$	
$\omega_0 = 1$ $x = -1$	F (0)	0.2326(0)	0.2322(0)	0.2%	0.2193(0)	5.7%
	F (τ^*)	0.3942(0)	0.3999(0)	1.4%	0.4128(0)	4.7%
	$\bar{I}(0)$	0.1413(0)	0.1428(0)	0.4%	0.9498(-1)	32.8%
	$\bar{I}(\tau^*)$	0.1944(0)	0.2020(0)	3.9%	0.1787(0)	8.1%
$\omega_0 = 1$ $x = .5$	F (0)	0.2895(0)	0.2869(0)	0.9%	0.2848(0)	1.6%
	F (τ^*)	0.3374(0)	0.3452(0)	2.3%	0.3473(0)	2.9%
	$\bar{I}(0)$	0.1661(0)	0.1659(0)	0.1%	0.1233(0)	25.8%
	$\bar{I}(\tau^*)$	0.1696(0)	0.1789(0)	5.5%	0.1504(0)	11.3%
$\omega_0 = 1$ $x = -1$	F (0)	0.4181(0)	0.4102(0)	1.9%	0.4285(0)	2.5%
	F (τ^*)	0.2086(0)	0.2220(0)	6.4%	0.2036(0)	2.4%
	$\bar{I}(0)$	0.223(0)	0.2177(0)	2.1%	0.1856(0)	16.5%
	$\bar{I}(\tau^*)$	0.1133(0)	0.1270(0)	12.1%	0.8816(-1)	22.2%
$\omega_0 = .5$ $x = .1$	F (0)	0.5119(-1)	0.5010(-1)	2.1%	0.5892(-1)	15.1%
	F (τ^*)	0.1205(0)	0.1236(0)	2.6%	0.1390(0)	15.4%
	$\bar{I}(0)$	0.3643(-1)	0.3516(-1)	3.5%	0.2551(-1)	30.0%
	$\bar{I}(\tau^*)$	0.5721(-1)	0.6000(-1)	4.9%	0.6021(-1)	5.2%
$\omega_0 = .5$ $x = .5$	F (0)	0.7591(-1)	0.7402(-1)	2.5%	0.8699(-1)	14.6%
	F (τ^*)	0.9844(-1)	0.1016(0)	3.2%	0.1138(0)	15.6%
	$\bar{I}(0)$	0.4676(-1)	0.4491(-1)	4.0%	0.3767(-1)	19.4%
	$\bar{I}(\tau^*)$	0.4817(-1)	0.5107(-1)	6.0%	0.4929(-1)	2.3%
$\omega_0 = .5$ $x = -1$	F (0)	0.1404(0)	0.1361(0)	3.1%	0.1589(0)	13.2%
	F (τ^*)	0.4165(-1)	0.4495(-1)	7.9%	0.5026(-1)	20.7%
	$\bar{I}(0)$	0.7375(-1)	0.7023(-1)	4.8%	0.6880(-1)	6.7%
	$\bar{I}(\tau^*)$	0.2495(-1)	0.2814(-1)	12.8%	0.2176(-1)	12.8%

TABLE 6

CASES OF ANISOTROPIC SCATTERING WITH PHASE FUNCTION

$$p(\mu, \mu') = \omega_0(1 + x\mu\mu') \text{ and } \tau^* = 4 \text{ and } \mu_0 = 1.$$

		Exact	Variational $\Delta\%$		2-Stream $\Delta\%$	
$\omega_0 = 1$ $x = 1$	$F^+(0)$	0.5728(0)	0.5718(0)	0.2%	0.5893(0)	2.9%
	$F^+(\tau^*)$	0.3834(0)	0.4099(0)	6.9%	0.3924(0)	2.3%
	$\bar{I}(0)$	0.2902(0)	0.2988(0)	3.0%	0.2552(0)	12.1%
	$\bar{I}(\tau^*)$	0.1674(0)	0.1897(0)	13.3%	0.1699(0)	1.5%
$\omega_0 = 1$ $x = .5$	$F^+(0)$	0.6286(0)	0.6256(0)	0.5%	0.6503(0)	3.5%
	$F^+(\tau^*)$	0.3256(0)	0.3561(0)	9.4%	0.3314(0)	1.8%
	$\bar{I}(0)$	0.3143(0)	0.3213(0)	2.2%	0.2816(0)	10.4%
	$\bar{I}(\tau^*)$	0.1424(0)	0.1668(0)	17.1%	0.1435(0)	0.8%
$\omega_0 = 1$ $x = -1$	$F^+(0)$	0.7293(0)	0.7224(0)	0.9%	0.7581(0)	3.9%
	$F^+(\tau^*)$	0.2201(0)	0.2592(0)	17.8%	0.2236(0)	1.6%
	$\bar{I}(0)$	0.3577(0)	0.3617(0)	1.1%	0.3283(0)	8.2%
	$\bar{I}(\tau^*)$	0.9681(-1)	0.1253(0)	29.4%	0.9683(-1)	0.0%
$\omega_0 = .5$ $x = 1$	$F^+(0)$	0.6122(-1)	0.5701(-1)	6.9%	0.7348(-1)	20.0%
	$F^+(\tau^*)$	0.2417(-1)	0.2758(-1)	14.1%	0.2371(-1)	1.9%
	$\bar{I}(0)$	0.4040(-1)	0.3626(-1)	10.2%	0.3182(-1)	21.2%
	$\bar{I}(\tau^*)$	0.9600(-1)	0.1151(-1)	19.9%	0.1026(-1)	6.9%
$\omega_0 = .5$ $x = .5$	$F^+(0)$	0.8927(-1)	0.8221(-1)	7.9%	0.1041(0)	16.6%
	$F^+(\tau^*)$	0.1839(-1)	0.2129(-1)	15.8%	0.1832(-1)	0.4%
	$\bar{I}(0)$	0.5194(-1)	0.4617(-1)	11.1%	0.4508(-1)	13.2%
	$\bar{I}(\tau^*)$	0.7407(-2)	0.9068(-2)	22.4%	0.7931(-2)	7.1%
$\omega_0 = .5$ $x = -1$	$F^+(0)$	0.1590(0)	0.1437(0)	9.6%	0.1792(0)	12.7%
	$F^+(\tau^*)$	0.6655(-2)	0.8427(-2)	26.6%	0.7544(-2)	13.4%
	$\bar{I}(0)$	0.8076(-1)	0.7035(-1)	12.9%	0.7761(-1)	3.9%
	$\bar{I}(\tau^*)$	0.2981(-2)	0.4094(-2)	37.3%	0.3266(-2)	9.6%

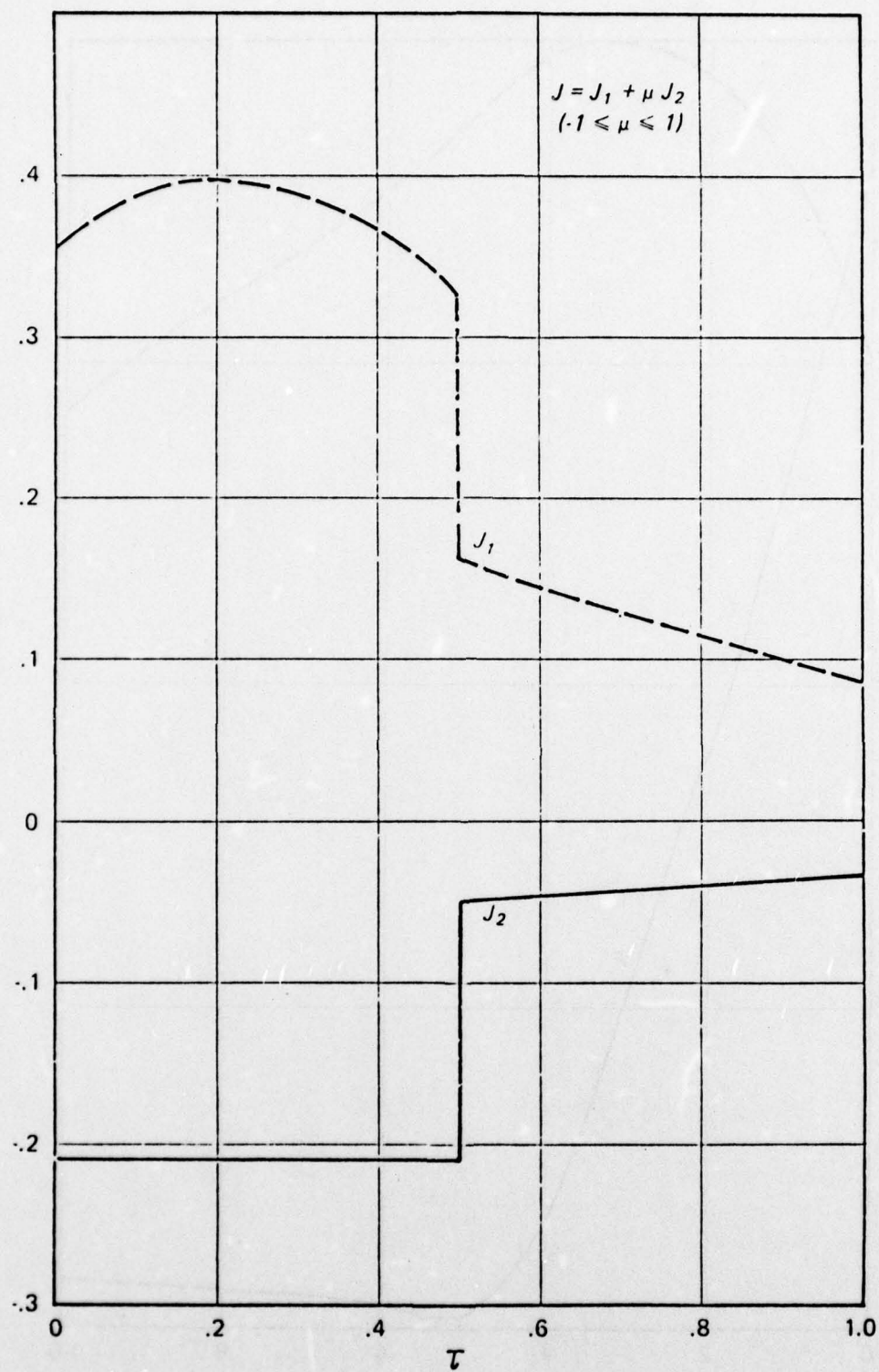


Figure 1A. Source Function Profile
 $\tau = 0 - 0.5, \omega_0 = 1, x = 1$
 $\tau = 0.5 - 1, \omega_0 = 0.5, x = 0.5$

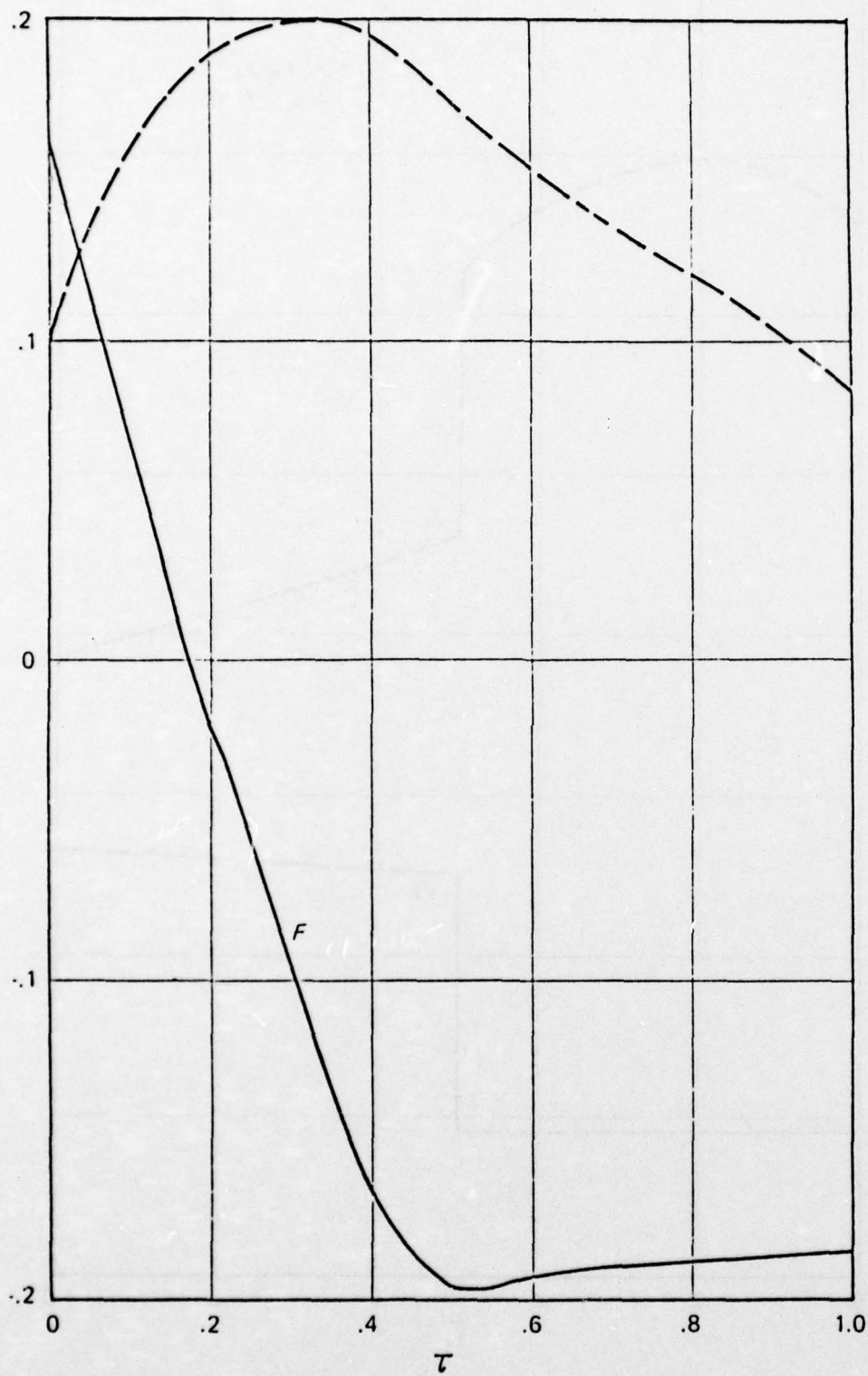


Figure 1B. Mean Intensity (\bar{I}) and Diffused Flux (F) Derived from Source Function in Figure 1A.

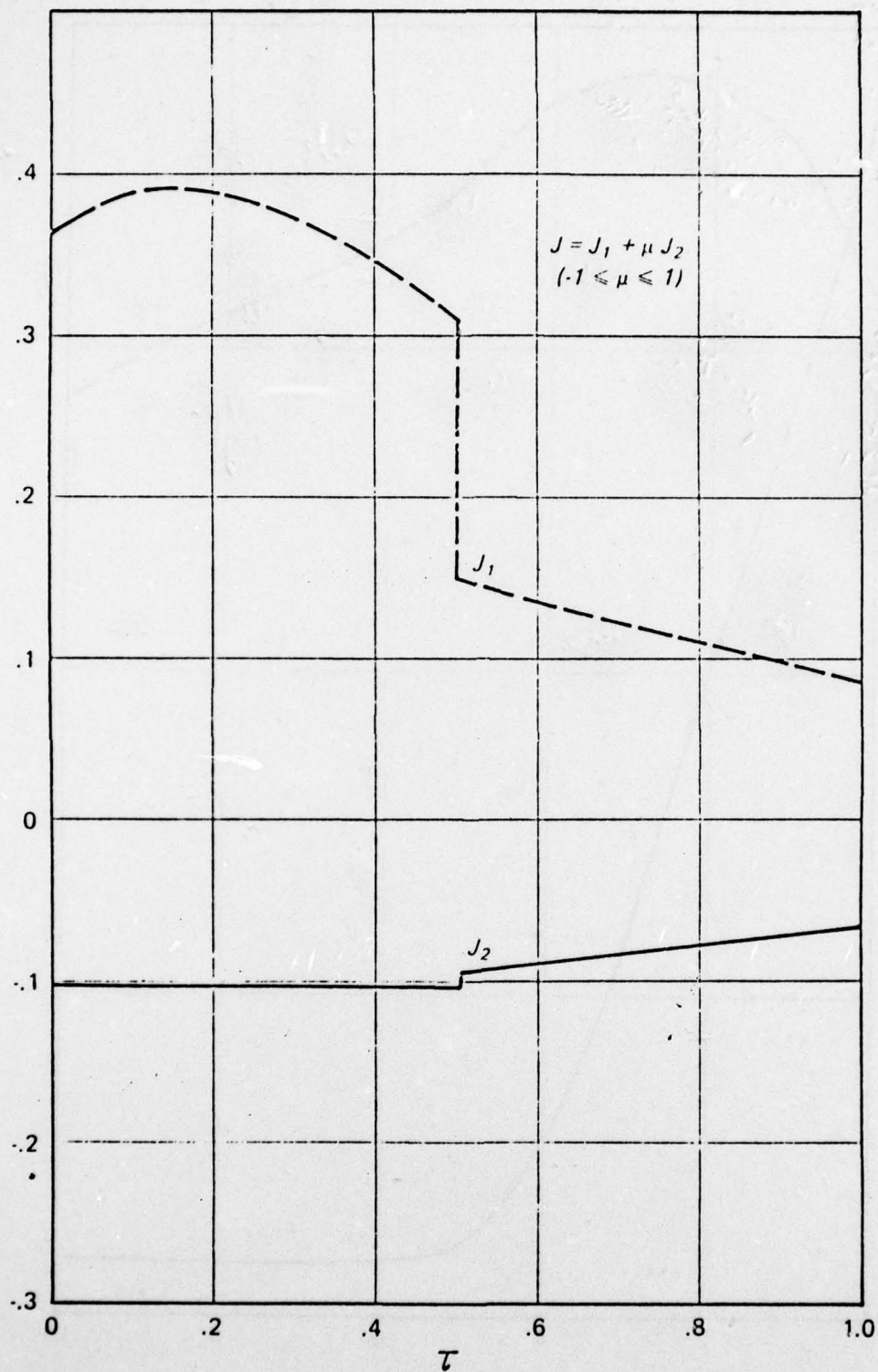


Figure 2A. Source Function Profile
 $\tau = 0 - 0.5, \omega_0 = 1, x = 0.5$
 $\tau = 0.5 - 1, \omega_0 = 0.5, x = 1$

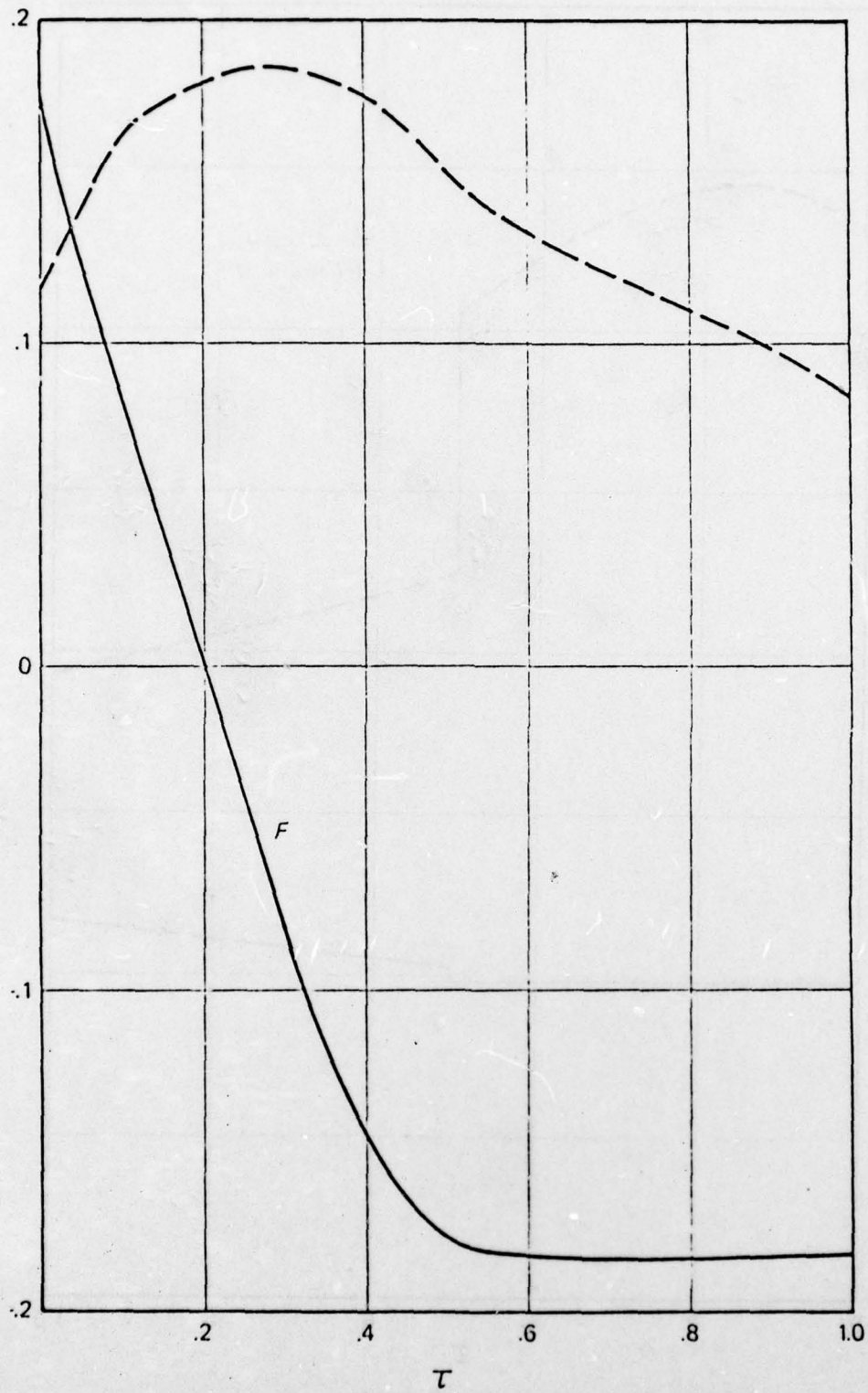


Figure 2B. Mean Intensity (\bar{I}) and Diffused Flux (F)
Derived from Source Function in Figure 2A.

an atmosphere of total optical depth (τ^*) of 1 divided into two regions such that from $\tau=0$ to 0.5, $\omega_0 = 1$ and from $\tau = 0.5$ to 1.0, $\omega_0 = .5$. In Figure 1, $X = 1$ and 0.5 for the respective regions and in Figure 2, $X = 0.5$ and 1. Figures 1A and 2A are the source function profiles. Figures 1B and 2B are corresponding profiles of the mean intensity (\bar{I}) and diffused flux (F).

Joseph et al. (1976) developed a Delta-Eddington approximation to transform the Henyey-Greenstein phase function into the form of $1 + X\cos\theta$ ($X = 3g$). We adopted this transformation to solve for different atmospheric conditions for which the Henyey-Greenstein phase function is used.

The Henyey-Greenstein phase function $p_{H-G}(\cos\theta)$ is defined as

$$p_{H-G}(\cos\theta) = \frac{1 - g^2}{(1 + g^2 - 2g\cos\theta)^{2/3}} \quad (51)$$

in which $g = \langle\cos\theta\rangle$ is the asymmetry factor. Different g values represent variously peaked phase functions. It can vary from -1 (complete back scattering) through 0 (isotropic scattering) to $g = 1$ (fully forward scattering). The Henyey-Greenstein phase function is a useful phase function because it applies to a variety of different atmospheres. Haze has asymmetry factor $g \sim 0.75$. Cloud droplets and aerosol particulates have g factors between 0.85 and 0.95 for most of the solar spectrum.

The Legendre polynomial expansion of the H-G phase function is shown to have the simple form (van de Hulst, 1968):

$$p_{H-G}(\cos\theta) \approx \sum_{\ell=0}^{\infty} (2\ell + 1)g^{\ell}P_{\ell}(\cos\theta) \quad (52)$$

where $P_{\ell}(\cos\theta)$ is the Legendre polynomial expansion. The Delta-Eddington approximation is a special combination of the Eddington and forward-peak-truncation approximations. It can be written as

$$\begin{aligned} p_{H-G}(\cos\theta) &\approx p_{\delta\text{-edd}}(\cos\theta) \\ &\equiv 2f\delta(1-\cos\theta) + (1-f)(1+3g'\cos\theta) \\ &= 1 + 3g\cos\theta + \sum_{\ell=0}^{\infty} (2\ell + 1)g^{\ell}P_{\ell}(\cos\theta) \end{aligned} \quad (53)$$

where f is the fractional scattering into the forward peak and g' is the asymmetry factor of the truncated phase function. f and g are shown to be

$$f = g^2 \quad (54)$$

and
$$g' = \frac{g}{1+g} \quad (55)$$

The Delta-Eddington phase function agrees with that of the H-G out to three terms and their difference is

$$P_{\delta\text{-edd}}(\cos \theta) - P_{\text{H-G}}(\cos \theta) = \sum_{\ell=3}^{\infty} (2\ell-1)(g^2-g^{\ell})P_{\ell}(\cos \theta) \quad (56)$$

The error in the phase function tends to grow smaller as $g \rightarrow 1$. At $g = 1$ (total forward scattering), the Delta-Eddington approximation is actually exact. By redefining

$$\omega'_0(\tau) \equiv \frac{(1-f)\omega_0(\tau)}{1-f\omega_0(\tau)} \quad (57)$$

$$\tau' \equiv (1-f\omega_0(\tau))\tau \quad (58)$$

and
$$I'(\tau', \mu) \equiv I\left(\frac{\tau'}{1-f\omega_0(\tau)}, \mu\right) = I(\tau, \mu) \quad (59)$$

we obtain the transformed set of the radiative transfer equation and the coupled integral equations for the source function.

Tables 7 and 8 show results of some of the tested cases. The doubling method was assumed to yield exact solution for comparison on the accuracies. Asymmetry factor $g = 0.75$ is used. $\omega_0 = 1$ and 0.8 represent fully and partially scattering atmospheres. $\tau^* = 0.25, 1$ and 4 are typical of thin, medium, and thick atmospheres. $\mu_0 = 0.9$ and 0.5 are chosen for near-normal and grazing solar incidences. The quantities presented are diffused fluxes at the top and bottom of the atmosphere ($F^+(0)$ and $F^+(\tau^*)$ respectively).

The results show that, despite the truncation in the phase function the percentage error is relatively small. It is thus conceivable to employ our method in real cloud conditions where anisotropy is non-negligible. In the next section we will discuss some examples of cirrus clouds in different wavelength ranges.

TABLE 7

τ^*	μ_0	F	Exact	Variational -iterative	Error %
0.25	0.9	$F^\uparrow(0)$ $F^\downarrow(\tau^*)$	0.2025(-1) 0.1980	0.2375(-1) 0.1945	17.3% 1.8%
	0.5	$F^\uparrow(0)$ $F^\downarrow(\tau^*)$	0.3590(-1) 0.1608	0.3455(-1) 0.1620	3.4% 0.7%
1	0.9	$F^\uparrow(0)$ $F^\downarrow(\tau^*)$	0.8703(-1) 0.5167	0.9420(-1) 0.5076	8.2% 1.8%
	0.5	$F^\uparrow(0)$ $F^\downarrow(\tau^*)$	0.1202 0.3121	0.1135 0.3189	5.6% 2.1%
4	0.9	$F^\uparrow(0)$ $F^\downarrow(\tau^*)$	0.3134 0.5760	0.3145 0.5673	0.3% 1.5%
	0.5	$F^\uparrow(0)$ $F^\downarrow(\tau^*)$	0.2597 0.2402	0.2546 0.2421	1.9% 0.8%

Accuracy of the VI Technique (Doubling Method is used to obtain exact solutions. Phase function is that of the H-G with Delta-Eddington transformation and $\omega_0 = 1$, $g = 0.75$.)

TABLE 8

τ^*	μ_0	F	Exact	Variational -iterative	Error %
0.25	0.9	$F^\dagger(0)$	0.1392(-1)	0.1589	14.1%
		$F^\dagger(\tau^*)$	0.1523	0.1491	2.1%
	0.5	$F^\dagger(0)$	0.2428(-1)	0.2405(-1)	1.0%
		$F^\dagger(\tau^*)$	0.1205	0.1225	1.7%
1	0.9	$F^\dagger(0)$	0.4437(-1)	0.4710(-1)	6.0%
		$F^\dagger(\tau^*)$	0.3497	0.3421	2.2%
	0.5	$F^\dagger(0)$	0.6171(-1)	0.6078(-1)	1.5%
		$F^\dagger(\tau^*)$	0.1904	0.1980	4.0%
4	0.9	$F^\dagger(0)$	0.8033(-1)	0.8163(-1)	1.6%
		$F^\dagger(\tau^*)$	0.2078	0.1864	10.3%
	0.5	$F^\dagger(0)$	0.8307(-1)	0.8395(-1)	1.1%
		$F^\dagger(\tau^*)$	0.5342(-1)	0.5359(-1)	0.3%

Accuracy of the VI Technique (Doubling Method is used to obtain exact solutions. Phase function is that of the H-G with Delta-Eddington transformation and $\omega_0 = 0.8$, $g = 0.75$.)

3.3.2 The Effects of Multiple Scattering on Microwave Brightness Temperature Observations

Three different tropical cloud (with rain) models are considered in the simulation of microwave brightness temperature values, one being single layer and the other two multilayer. An ocean background with a surface temperature of 300°K is assumed.* Surface reflectivities of 0.6 for 19.35 GHz and 0.552 for 37 GHz are used.

The optical depth and single scattering albedo values were calculated from the given profiles of volume extinction and absorption coefficients of water vapor, oxygen and cloud droplets. The optical depth and single scattering albedo profiles obtained are then approximated by different step functions (average step size is $\Delta\tau \sim 0.2$) where each step is assigned a fixed value of single scattering albedo. The source function profile is then obtained by applying the variational-iterative technique. The brightness temperature (proportional to the outgoing radiance) is thus calculated from (16) for different look angles. Tables 9 to 11 show the resultant brightness temperature for each of the cloud cover cases considered.

The contribution of emission from the atmosphere and clouds (first term in (16)) is always the least for $\mu = 1$ (normal look down angle), and increases for decreasing μ . The opposite is true for surface emission and reflection (second and third terms in (16)). Furthermore, the contribution from the background surface, both emission and reflection, drops exponentially as a function of the total optical thickness. As a result, for an optically thick atmosphere (e.g. Table 11B) the total brightness temperature is the greatest at $\mu = 1$ because surface emission and reflection terms are appreciable only near $\mu = 1$ and angular dependence on the atmospheric emission is less significant. For thinner atmospheres on the other hand, the total brightness temperature is the least at $\mu = 1$ due to the relatively small contribution of the atmospheric emission near $\mu = 1$ (e.g. Tables 9, 10 and 11A).

The results are also compared with those from the ERT Radiative Absorption and Scattering Program (RASP) with the same cloud conditions applied. The main difference between the two models is that RASP does not handle multiple scattering through the source function; the source function is simply the Planck's function ($J(\tau) = B(T(\tau))$) in which

TABLE 9

One layer tropical cloud (0-4000 m)
Liquid water content = 0.045 gm/m^3
Mode radius = 400μ
Surface temperature = 300°K

- A. Frequency 19.35 GHz
Surface albedo = 0.6
Total optical depth = 0.3 (0.14 without cloud)
Single scattering albedo up to 4000 m = 0.15 to 0.22

Brightness Temperature Calculated:

μ	Atm. Emi.	Surf. Ref.	Surf. Emi.	Total
0.2	201.9	14.2	26.8	242.9
0.4	138.3	30.2	56.7	225.1
0.6	103.4	38.7	72.8	214.9
0.8	82.3	43.9	82.5	208.7
1.0	68.3	47.3	88.9	204.5

Unit: $^\circ\text{K}$

- B. Frequency 37.0 GHz
Surface albedo = 0.552
Total optical depth = 0.5 (0.16 without cloud)
Single scattering albedo up to 4000 m = 0.37 to 0.46

Brightness Temperature Calculated:

μ	Atm. Emi.	Surf. Ref.	Surf. Emi.	Total
0.2	205.8	6.0	11.0	222.8
0.4	163.6	21.1	38.5	223.2
0.6	130.7	32.0	58.4	221.1
0.8	107.9	39.4	71.4	219.2
1.0	91.6	44.6	81.5	217.7

Unit: $^\circ\text{K}$

TABLE 10

Five layer tropical cloud I

(0-2000 m, 2000 m - 4000 m, 4000 m - 6000 m, 6000 - 8000 m,
8000 - 10,000 m)

Liquid water content = 0.060, 0.050, 0.030, 0.020 and 0.020 gm/m³
respectively

Mode radius = 450, 400, 350, 300, 200 μ respectively

Surface Temperature = 300°K

A. Frequency 19.35 GHz

Surface albedo = 0.6

Total optical depth = 0.24 (0.15 without cloud)

Single scattering up to 10,000 m = 0.009 to 0.044

Brightness Temperature Calculated:

μ	Atm. Emi.	Surf. Ref.	Surf. Emi.	Total
0.2	192.1	17.3	36.1	245.5
0.4	124.9	31.4	65.9	222.2
0.6	91.5	38.4	80.4	210.3
0.8	72.0	42.5	88.9	203.4
1.0	59.3	45.1	94.4	198.8

Unit: °K

B. Frequency 37.0 GHz

Surface albedo = 0.552

Total optical depth = 0.52 (0.17 without cloud)

Single scattering albedo up to 10,000 m = 0.03 to 0.23

Brightness Temperature Calculated:

μ	Atm. Emi.	Surf. Ref.	Surf. Emi.	Total
0.2	242.8	6.3	10.0	259.1
0.4	193.1	23.2	36.5	252.9
0.6	154.5	35.8	56.5	246.8
0.8	127.7	44.5	70.2	242.3
1.0	108.4	50.7	79.9	239.0

Unit: °K

TABLE 11

Five layer tropical cloud II
(0 - 2000 m, 2000 m - 4000 m, 4000 m - 6000 m, 6000 m - 8000 m,
8000 - 10,000 m)
Liquid water content = 0.360, 0.300, 0.180, 0.130, 0.100 gm/m³,
respectively
Mode Radius = 450, 400, 350, 300, 200 μ , respectively
Surface temperature = 300°K

- A. Frequency 19.35 GHz
Surface albedo = 0.6
Total optical depth = 0.71 (0.15 without cloud)
Single scattering albedo up to 10,000 m = 0.01 to 0.086

Brightness Temperature Calculated:

μ	Atm. Emi.	Surf. Ref.	Surf. Emi.	Total
0.2	259.0	3.4	3.6	266.0
0.4	224.8	19.6	20.9	265.3
0.6	188.6	35.1	37.4	261.1
0.8	160.5	47.0	50.0	257.5
1.0	138.7	56.0	59.6	254.3

Unit: °K

- B. Frequency 37.0 GHz
Surface albedo = 0.552
Total optical depth = 2.24 (0.17 without cloud)
Single scattering albedo up to 10,000 m = 0.03 to 0.32

Brightness Temperature Calculated:

μ	Atm. Emi.	Surf. Ref.	Surf. Emi.	Total
0.2	251.5	0.0	0.0	251.5
0.4	256.8	0.6	0.5	257.9
0.6	255.9	3.6	3.2	262.7
0.8	249.0	9.1	8.2	266.3
1.0	238.6	16.0	14.3	268.9

Unit: °K

scattering cross sections are included for calculation of the optical depth. Another difference is the handling of the surface reflection terms. In the VI program, the Lambertian surface approach is adopted. Reflectivity of the surface is defined as the ratio between the incoming and outgoing fluxes at the surface and the reflection is isotropic (i.e. no angle preference for the outgoing radiance) (equ. (14)). In RASP, the specular reflection condition is used, or

$$I(\tau^*, \mu) = R I(\tau^*, -\mu) \quad (60)$$

As a result, because the atmospheric emission term is generally higher for smaller μ 's, at $\mu = 1$ (normal look down angle) the Lambertian model, which takes incoming radiation from all angles into consideration, gives a higher surface reflection term than that of the specular reflection.

Comparisons are carried out for the same clouds at $\mu = 1$, the angle which RASP operates specifically. Specular reflection at the surface for the VI model is included to demonstrate the difference between different reflection models. The results of different approaches are shown in Table 12.

It is shown from the last two columns in Table 12 that the difference in the brightness temperatures between specular and Lambertian surface reflections generally lies between 15 and 20 degrees except for the thick atmosphere case ($\tau^* = 2.24$) where the difference is only 4 degrees because in this case the angular dependence on the atmospheric emission term is not significant (Table 11B).

Results of RASP and VI techniques are also compared for the same surface model. It is shown (Table 12) that the two models agree quite well for small single scattering albedos ($\omega_0 \leq 0.05$). When appreciable scattering is present, RASP tends to overestimate the brightness temperature for thinner atmospheres because the scattering term (second term in (15)) is less than $\omega_0 B$. On the other hand, RASP also may underestimate the brightness temperature when the optical depth is higher for the more complex conditions specified in Table 11.

TABLE 12

Summary of Atmospheric Conditions			Brightness Temperature ($^{\circ}\text{K}$)		
τ^*	ω_0	R	RASP (specular ref)	VI (specular ref)	VI (Lambertian)
0.3	0.15-0.22	0.6	195.4	186.1	204.5
0.5	0.31-0.46	0.552	232.4	198.3	217.7
0.24	0.009-0.044	0.6	182.2	181.2	198.8
0.52	0.03-0.23	0.552	209.2	221.5	239.0
0.71	0.01-0.086	0.6	232.9	237.9	254.3
2.24	0.03-0.32	0.552	233.5	264.1	268.9

$$\mu = 1$$

3.3.3 Anisotropic Scattering through Cirrus Cloud Layers in the Visible and Infrared Regions

The major difficulty of scattering computation for cirrus clouds arise from the random distribution of the highly nonspherical ice crystals in the cloud layers. Little information, either theoretical or observational, on the composition of the cirrus clouds is known. However, though geometrically thin (≤ 500 m), they are usually optically thick which makes the determination of the atmospheric structure from orbiting meteorological satellites difficult.

A preliminary study of the scattering problem through cirrus clouds has been performed. We adopted Liou's (1972) computations of the phase function, the single scattering albedo and the extinction cross-section (β_{ext}) of cirrus cloud layers for some sample wavelengths (0.7μ , 3μ , and 10μ). The assumption is that the ice crystals in cirrus clouds can be approximated by long circular cylinders which are randomly oriented in space. Table 13 is a summary of the optical properties (ω_0 , g , β_{ext}) of randomly oriented ice crystals at the sample wavelengths. We then chose three cirrus cloud layers with different thicknesses: 100 m for a very thin layer, 200 m for a medium thin layer, and 500 m for a relatively thick cirrus cloud layer. The total optical depth of each layer is simply the product of the volume extinction cross-section (β_{ext}) and the geometric thickness.

Tables 14, 15, and 16 are results for $\lambda = 0.7 \mu$, 3μ and 10μ respectively. Cosines of solar zenith angles (μ_0) of 0.9 and 0.5 are chosen as cases for near-normal and grazing solar incidences. Quantities presented are reflection (r) and transmission (t) as defined as

$$r = \pi F \uparrow(0) / \pi \mu_0 F_0 \quad (61)$$

$$\text{and} \quad t = \pi F \uparrow(\tau^*) / \pi \mu_0 F_0 + \exp(-\tau^* / \mu_0) \quad (62)$$

where πF is the unattenuated solar flux. Results with isotropic scattering ($g = 0$) for the same cases are also included to demonstrate the effect of forward scattering of the ice crystals.

As expected, $g > 0$ (forward scattering) always increases the transmission and decreases the reflection as compared to $g = 0$. It is also shown that in the visible range, most of the light gets transmitted through

TABLE 13

$\lambda (\mu)$	$\tilde{\omega}_0$	g	$\beta_{\text{ext}} (\text{km}^{-1})$	τ^*		
				100 m	200 m	500 m
0.7	1.0	0.73	3.3	0.33	0.65	1.6
3	0.5	0.65	20	2	4	10
10	0.5	0.87	20	2	4	10

Optical Properties for Cirrus Cloud Layers of Different Thicknesses at Different Wavelengths

TABLE 14

Thickness	μ_o	r	$r^1(\text{isotropic})$	t	$t^1(\text{isotropic})$
100 m	0.9	0.3669(-1)	0.1554	0.9629	0.8446
	0.5	0.9253(-1)	0.2470	0.9069	0.7530
200 m	0.9	0.7380(-1)	0.2663	0.9257	0.7337
	0.5	0.1687	0.3858	0.8307	0.6142
500 m	0.9	0.1811	0.4621	0.8155	0.5379
	0.5	0.3343	0.5652	0.6629	0.4348

Reflection (r) and Transmission (t) through
Different Cirrus Cloud Layers at $\lambda = 0.7 \mu$

TABLE 15

Thickness	μ_0	r	r^1 (isotropic)	t	t^1 (isotropic)
100 m	0.9	0.3359(-1)	0.1074	0.2386	0.1706
	0.5	0.7217(-1)	0.1310	0.9527(-1)	0.7416(-1)
200 m	0.9	0.3415(-1)	0.1096	0.6760(-1)	0.2623(-1)
	0.5	0.7354(-1)	0.1320	0.2046(-1)	0.8386(-1)
500 m	0.9	0.3426(-1)	0.8783(-1)	0.5144(-3)	0.3317(-3)
	0.5	0.7441(-1)	0.9490(-1)	0.1081(-3)	0.8526(-4)

Reflection (r) and Transmission (t) through
Different Cirrus Cloud Layers at $\lambda = 3 \mu$

TABLE 16

Thickness	μ_o	r	r^1 (isotropic)	t	t^1 (isotropic)
100 m	0.9	0.9571(-2)	0.1074	0.3052	0.1706
	0.5	0.2948(-1)	0.1310	0.1266	0.7416(-1)
200 m	0.9	0.9832(-2)	0.1096	0.8085(-1)	0.2623(-1)
	0.5	0.3030(-1)	0.1320	0.1691(-1)	0.8386(-2)
500 m	0.9	0.9842(-2)	0.8783(-1)	0.2384(-2)	0.3317(-3)
	0.5	0.3053(-1)	0.9490(-1)	0.2753(-3)	0.8526(4)

Reflection (r) and Transmission (t) through
Different Cirrus Cloud Layers at $\lambda = 10 \mu$

the cloud layer. Furthermore, since $\omega_0 = 1$, a case of total scattering, there is no absorption through the cloud layer. (The fraction of absorption $a = 1 - r - t$.) However, into the IR region, except for very thin layers, most of the light is absorbed. Reflection or transmission is at most a few percent.

4. INFRARED RADIANCE SIMULATIONS WITH CLOUDS

The infrared radiance simulation package obtained from AFGWC and modified for use on the AFGL CDC 6600 computer was further modified to incorporate cloud scattering and the use of the VI technique for calculating the radiance values. The program was modified only to incorporate isotropic scattering, the effects of anisotropy being of second order relative to the effect of including scattering in the radiance calculations.

4.1 Software Modification

The simulation program RAPID GABTAWF (Weichel, 1976) was modified to include the VI algorithm for the multiple scattering effect rather than the numerical quadrature procedure assuming no scattering used by AFGWC. The transmittance values for the 70 levels of the AFGWC^t integration program were multiplied by the additional cloud contributions and the resultant weighting function profile was used to generate a new set of heights for the VI subroutine. The profile was divided into roughly 20 levels of nearly equal optical depth, each level being approximated by an averaged single scattering albedo. These levels were used for the multiple scattering computations and further iterations were applied for better accuracies.

4.2 Cloud Simulations

The variational-iterative technique was fully tested with realistic atmospheres and clouds using the CDC 6600 computer facilities at AFGL.

The effects of clouds were simulated using two cloud models: high-thin cirrus clouds and low level stratus clouds. These cases were chosen because they represent the conditions under which the normal cloud screening algorithms would fail. Table 17 shows the properties of these clouds including the cloud type, base and top altitudes, density and mode radius of the cloud droplets. In all cases, the clouds were assumed to completely fill the field of view. A radiosonde profile from Washington, D.C. (spring) with surface temperature of 283°K and emissivity of one was used. The refractive indices of ice and water were provided by the contract monitor, Mr. V.J. Falcone.

TABLE 17

	Cloud Type	Cloud Base (m)	Cloud Top (m)	Mode Radius (μ)	Density (gm/m ³)	τ_{tot}^*	ω	Cloud Top Temp ($^{\circ}$ K)	B and T _B (absp. only)	B and T _B (scatt. included)
A	thin stratus	150	650	10	.1	4.7	.439	278.5	95.6 279.4	91.0 276.3
B	thick stratus	150	2500	10	.1	22.3	.439	276.5	89.2 275.1	86.7 273.3
C	thin cirrus	5000	7000	40	.1	3.3	.532	244.8	54.2 247.1	51.0 244.1
D	thick cirrus	5000	11000	40	.1	10.0	.532	215.3	27.2 216.5	26.1 214.9
E	thin cirrus	5000	7000	40	.01	.33	.532	244.8	85.8 272.7	82.2 270.2
F	thick cirrus	5000	11000	40	.01	1.0	.532	215.3	44.4 237.5	43.0 236.0

*cloud only

Summary of Cloud Models and Their Optical Properties at 12 μ m(B in erg/sec/cm²/strd, T_B in $^{\circ}$ K)

Calculations for radiances were done at 8 IR channels with wavelengths of 15, 14.8, 14.4, 14.2, 13.8, 13.4, 12, and 18.7 microns, respectively. The 7th channel (12 micron) is a window channel which has high transmittance under clear atmospheric conditions. The optical properties of the clouds at this channel, τ_{tot} (total optical depth) and ω (single scattering albedo) are also presented in Table 17.

Results for various clouds are shown in Figures 3-8 for all eight channels. Radiances (B) are also converted to the equivalent black body temperature (T_B) defined by the Planck radiance function:

$$B = 2hc^2\lambda^{-5}/(\exp(hc/k\lambda T_B)-1) \quad (63)$$

where h is Planck's constant, c is the speed of light and λ is the wavelength. Computations were done both for pure absorption (the AFGWC model) and multiple scattering (VI).

It has been demonstrated that the VI technique is generally fast and relatively accurate. Tests were carried out using different layer thicknesses. It was shown that VI deals with thin atmospheres the best (in contrast to the Doubling Method and Discrete Ordinate Method). For thicker atmospheres, a larger number of layers and more iterations were required for the desired accuracy. It is also noted that for a discontinuous atmosphere (for example, a scattering cloud imbedded in a large, purely absorbing atmosphere) the model should include the multiple scattering (for the cloud) and pure absorption (for the rest of the atmosphere) computations simultaneously.

Results show that for channels 1 through 5 the atmosphere above the cloud is sufficiently opaque to mask the effects of multiple scattering within the cloud. In other words, a pure absorption treatment is adequate and the general assumption of brightness temperature equal to the cloud top temperature as used in Section 2 is valid for these channels.

Secondly, for all low stratus clouds, no scattering treatment is necessary except in the window channel (No. 7). This is verified by the facts that in these cases (1) there is little difference in radiance values between pure absorption and scattering computations, and (2) the equivalent black body temperature is always below the cloud top temperature indicating the already low transmittance values before entering the cloud top.

○ Scattering included
 X Absorption only

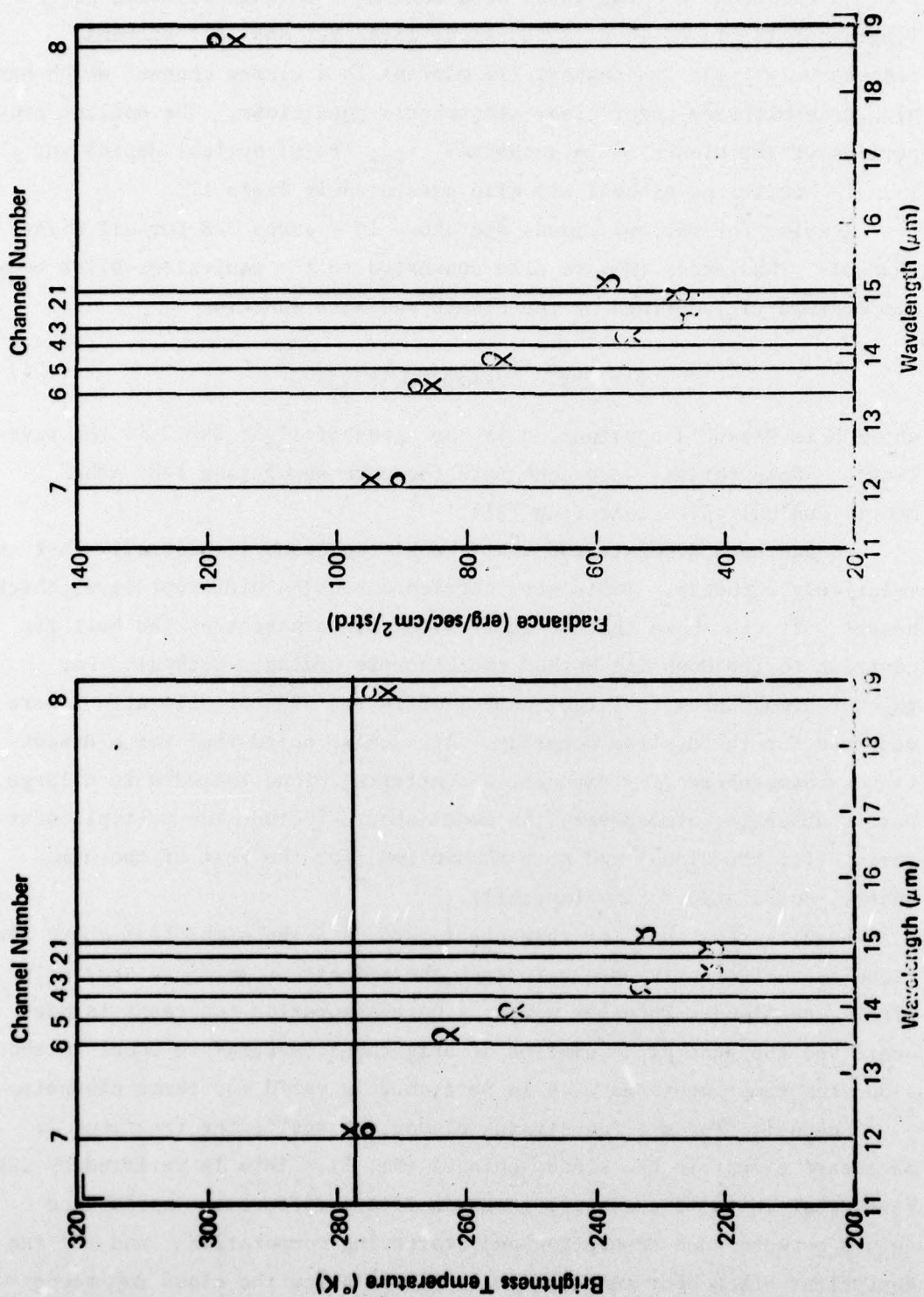


Figure 3. Brightness Temperatures and Radiances for Cloud Type A at All Eight IR Channels (— indicates the cloud top temperature)

○ Scattering included
 X Absorption only

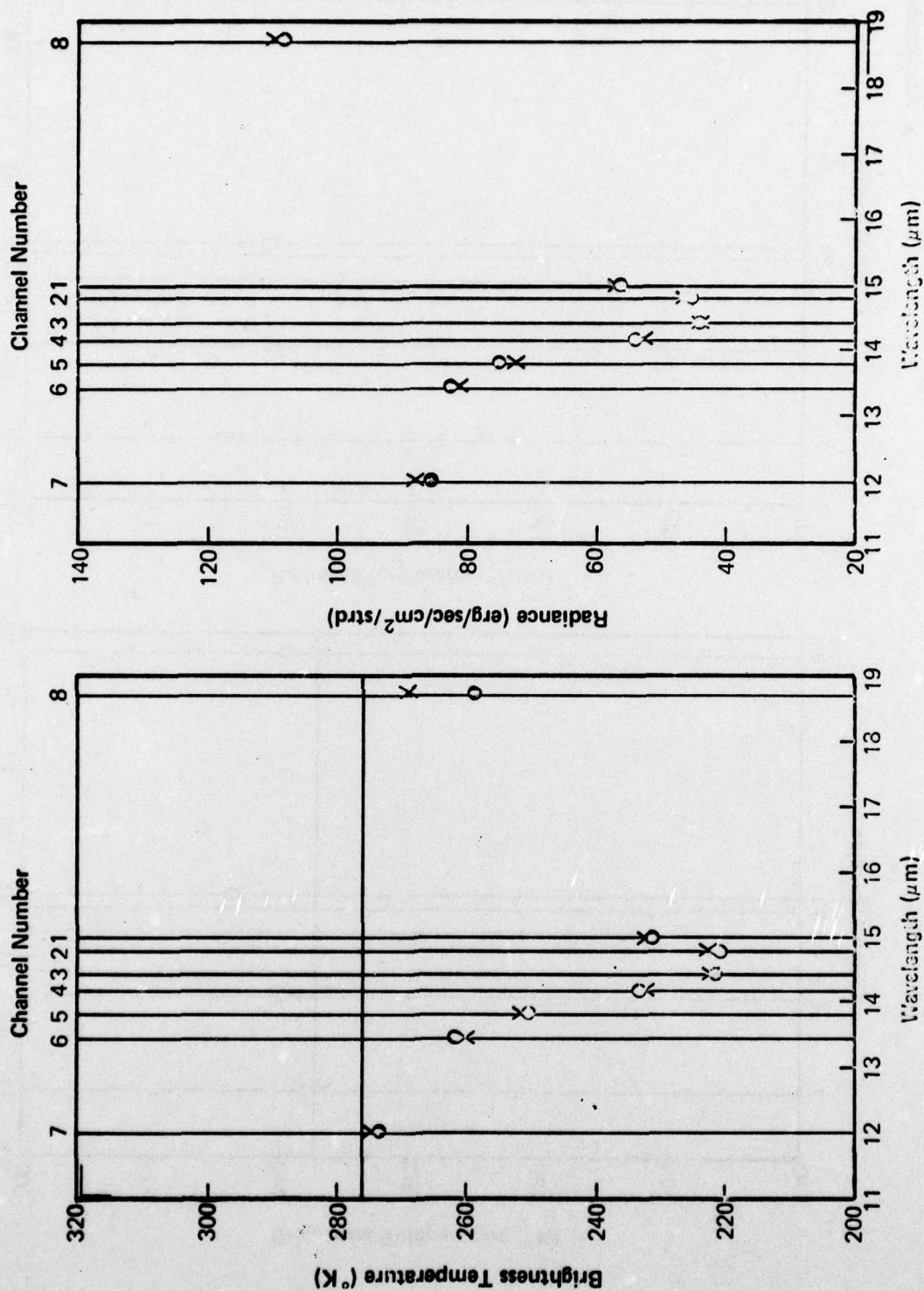


Figure 4. Brightness Temperatures and Radiance for Cloud Type B at All Eight IR Channels
 (— indicates the cloud top temperature)

○ Scattering included
 X Absorption only

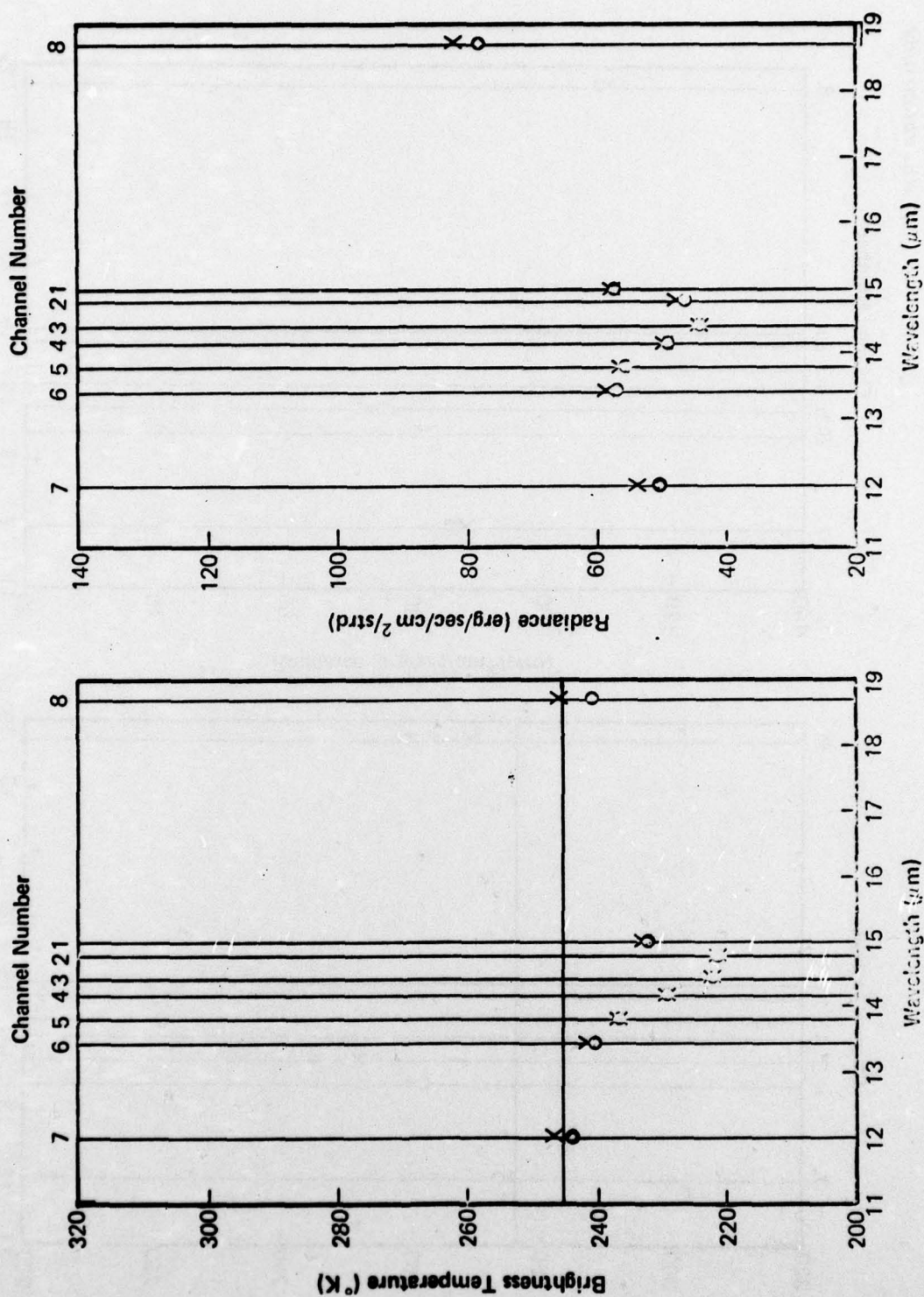


Figure 5. Brightness Temperatures and Radiance for Cloud Type C at All Eight IR Channels (— indicates the cloud top temperature)

○ Scattering included
 X Absorption only

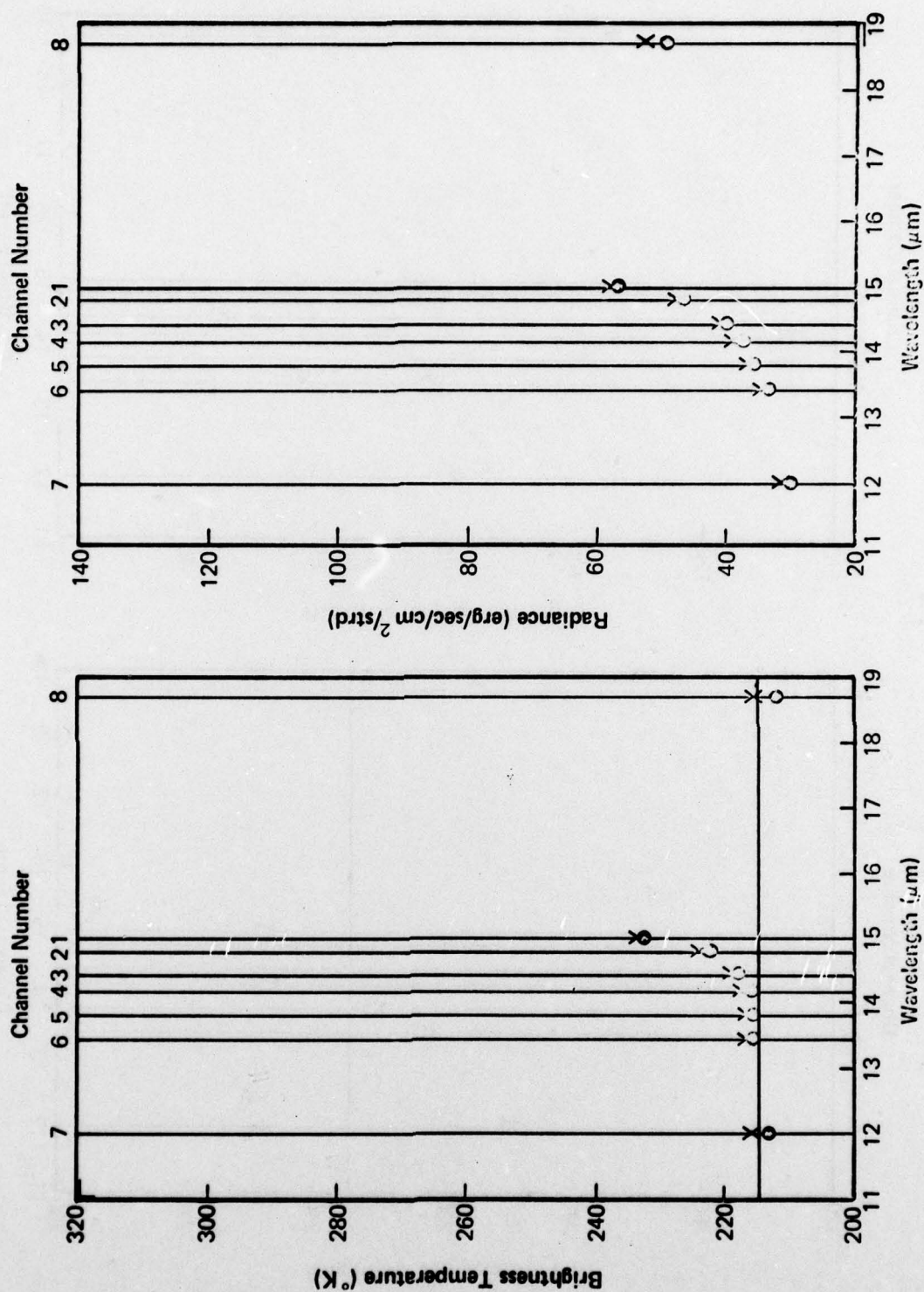


Figure 6. Brightness Temperatures and Radiances for Cloud Type D at All Eight IR Channels
 (—— indicates the cloud top temperature)

○ Scattering included
 X Absorption only

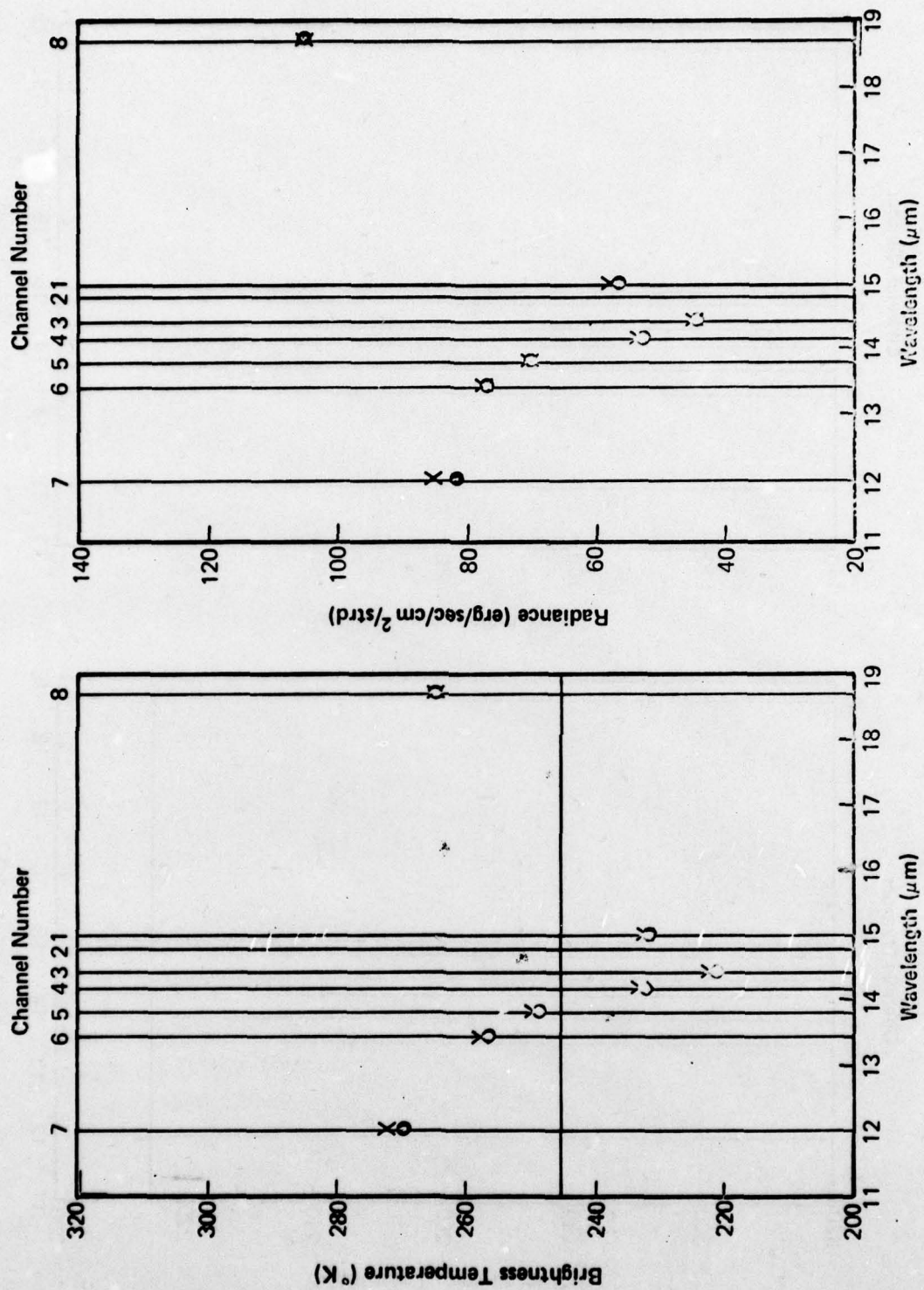


Figure 7. Brightness Temperatures and Radiances for Cloud Type E at All Eight IR Channels
 (— indicates the cloud top temperature)

• Scattering included
 X Absorption only

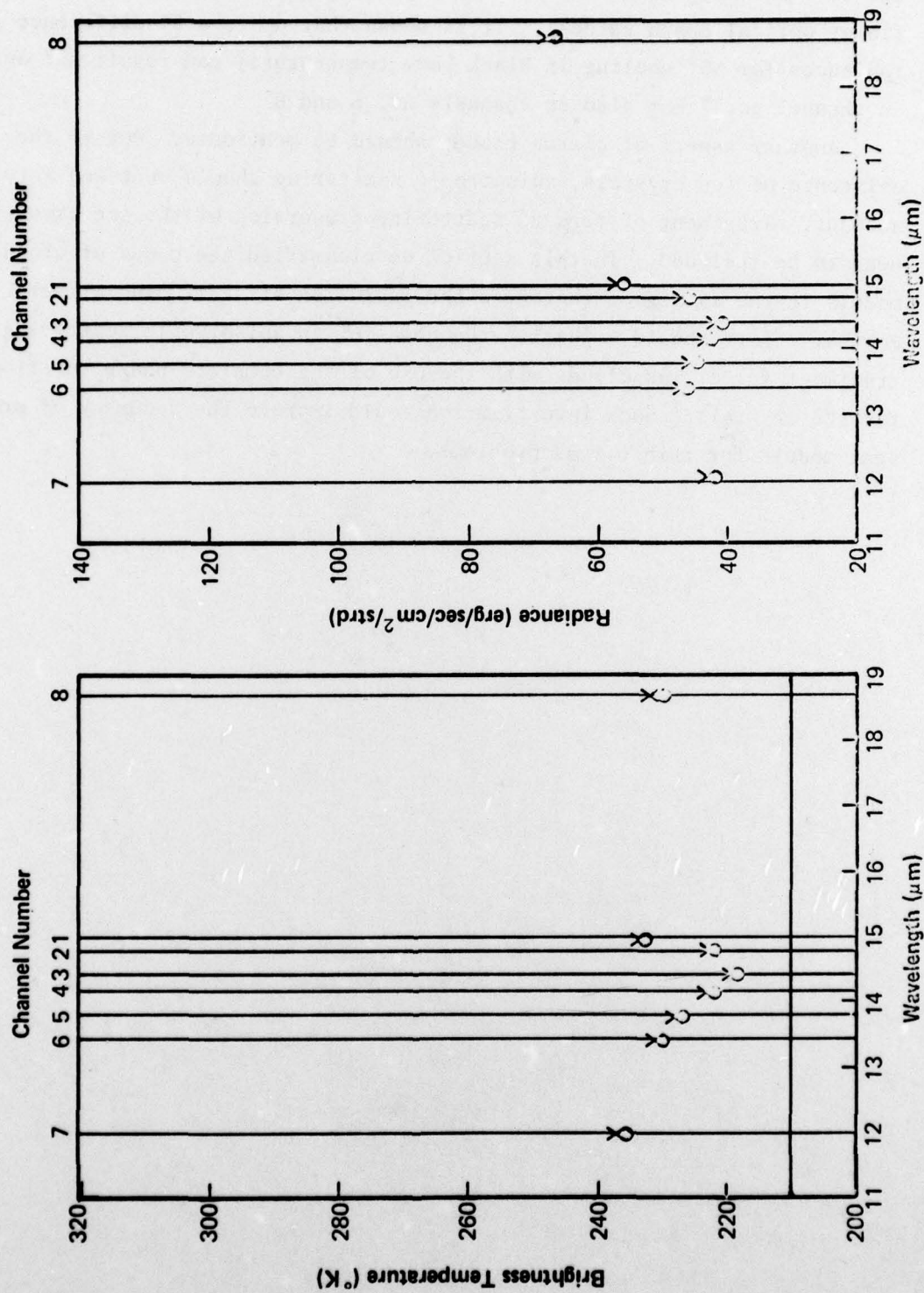


Figure 8. Brightness Temperatures and Radiance for Cloud Type F at All Eight IR Channels
 (— indicates the cloud top temperature)

Cirrus clouds, on the other hand, need multiple scattering treatment due to their high altitudes and the more transparent optical properties (lower optical depth values). It is shown that up to a 5% difference in radiances (or $\sim 3^\circ$ cooling in black body temperature) can result not only in channel no. 7 but also in channels no. 6 and 8.

Another aspect of cirrus clouds should be mentioned. Due to the existence of ice crystals, anisotropic scattering should be taken into account. Treatment of forward scattering properties of the ice crystals need to be included. In this section we classified the cases of cloud models in the IR region that need the inclusion of scattering effects. Further effort should emphasize the need for an anisotropic scattering treatment for cirrus clouds with the use of the complete phase functions for ice crystals. Such investigation would improve the accuracy of present models for thin cirrus problems.

5. PARTIAL CLOUDINESS IN THE FIELD-OF-VIEW

The variational-iterative procedure for obtaining a solution to the radiative transfer equation was developed for application to problems with axial symmetry about the zenith direction in a plane-parallel scattering atmosphere. This limitation is inherent in most of the rapid techniques for obtaining a solution to the radiative transfer equation. In the case of the variational-iterative technique, the restrictions may be relaxed but only at the expense of significantly increasing the dimensions of the matrices that must be inverted to obtain a solution. In special cases, this may provide more insight into the nature of multiple scattering problems but, in the general case of simulating brightness fields for horizontally homogeneous clouds, the application of this or any of the other plane-parallel atmosphere procedures is impractical.

The problem of obtaining temperature profiles from brightness measurements in the presence of clouds was reviewed in Section 2.3. The procedures used were based upon the assumption that the region with clouds could be subdivided into subregions with and without clouds and that the radiative transfer problem could be independently solved for each subregion. The total radiance observed at the satellite then could be obtained by summing the contributions from each region. Since the different regions contributed in proportion to their areas, the area weighted results, equation (4), is obtained.

The response of a satellite-borne radiometer to a horizontally inhomogeneous scene (surface brightness field) viewed through a horizontally inhomogeneous non-scattering atmosphere may be represented by the generalization of equation (1):

$$I_v \propto \iint_{\text{surface}} g(\xi, \eta) \{ B_v [T(P_s, X_s, Y_s)] \Theta_v(P_s, X_s, Y_s) - \int_0^{P_s} B[T(p, x, y)] \cdot \quad (64)$$

$$\frac{d\Theta_v(p, x, y)}{dp} dp \} dX_s dY_s$$

where ξ, η represent the angle subtended by the point X_s, Y_s as viewed from the satellite,

$g(\xi, \eta)$ is the intensity response of antenna gain of the optical or microwave system in the direction ξ, Y

and x, y represent the horizontal position of the ray between the satellite and P_s , X_s , Y_s at the pressure level P .

If the intensity response function, $g(\xi, \eta)$ is a delta function, then only radiation from a single direction ξ_0, η_0 is observed and equation (1) obtains. If the response function is narrow so the changes in the integrand specified by variations in X_s , Y_s , X , and Y are small in comparison with changes in $g(\eta, \xi)$, equation (1) still obtains. However, if the response function has a large field-of-view with a uniform response in each direction, $g(\xi, \eta) = \text{constant}$, then equation (64) corresponds to the area weighted response, equation (4).

The use of equation (64) to represent the area weighted cloud contribution requires the additional assumption that the clouds may be locally treated as plane-parallel scattering regions and the relative contributions of the edges are small (locally horizontally homogeneous). While this assumption can only be checked using the full radiative transfer equation and horizontally inhomogeneous model atmospheres, the uncertainties in the model clouds used to represent the atmosphere may be larger than the effects of the inhomogeneities. In the end, the use of equation (64) to investigate the effects of clouds depends upon assumptions about the clouds within the field-of-view and model clouds that are relatively much larger in the horizontal than vertical may be postulated that reasonably fulfill the requirements for local homogeneity. These clouds must be treated as effective clouds with properties inferred to correspond to observations.

6. CONCLUSIONS

The variational-iterative (V-I) procedure for the solution of the radiative transfer equation for a plane-parallel scattering atmosphere (multiple scattering) was modified and extended for use in problems involving anisotropic scattering. The V-I technique was incorporated in the AFGL simulation package for the DMSP infrared sounder. Application of the technique to conditions of high thin cirrus clouds or to low stratus clouds showed that the multiple scattering calculations are required to adequately simulate cloud effects in the window channel; the effect of multiple scattering was to produce a five percent difference in the simulated radiance value, a value large compared with the expected measurement noise.

A statistical analysis of the relative merits of the infrared only, microwave only, and infrared plus microwave sounder systems revealed that for cloud free skies, one system did as well as the other. In the presence of clouds and for microwave and infrared sounder systems with identical fields-of-view, the microwave sounder system was superior to the infrared system; the addition of infrared data to the microwave sounder data provided new information for the assessment of cloud cover and height but no new information for the deduction of temperature profiles. For the current and planned microwave sounder systems, the much larger field-of-view of the microwave system can be a disadvantage. Using current procedures for the evaluation of temperature profiles in the presence of clouds, the profile inferred from the infrared sounder is assumed to apply to a horizontal region significantly larger than the field-of-view of the infrared sensor. When the microwave sensor field-of-view matches the larger horizontal region of the infrared system in the presence of clouds, the microwave system is superior for temperature profiling and the infrared system should be used in combination with the microwave system for estimating cloud height and coverage.

REFERENCES

- Bengtsson, L., 1975: "4-Dimensional Assimilation of Meteorological Observations", GARP Publication Series No. 15, WMO, Geneva.
- Bunting, J.T., F.R. Valovcin and T.J. Keegan, 1977: Meteorological Satellite Measurements and Applications, AFGL-TR-77-0035, Air Force Geophysics Laboratory.
- Burke, H.K. and N.D. Sze, 1977: A Comparison of Variational and Discrete Ordinate Methods of Solving Radiative Transfer Problems, J. Quart. Spectro. Radiat. Transfer., 17, 783-793.
- Carstedt, J.L. and T.W. Mullikin, 1966: Ap. J. Suppl. 12, 449.
- Chandrasekhar, S., 1960: Radiative Transfer, Dover, New York.
- Crane, R.K., 1976: An Algorithm to Retrieve Water Vapor Information from Satellite Measurements, Final Report Contract N00 228-75-C-2378, Environmental Research & Technology, Inc.
- Gaut, N.E., E.C. Reifenshtein, III, and D.T. Chang, 1972: Microwave Properties of the Atmosphere, Clouds and the Oceans, Final Report, Contract NAS5-21194, Environmental Research & Technology, Inc.
- Joseph, J.H., W.J. Wiscombe and J.A. Weinman: The Delta-Eddington Approximation for Radiative Flux Transfer, J. Atmos. Sci., 33, 2452.
- Kourganoff, V., 1963: Basic Methods in Transfer Problems, Dover, New York.
- Liou, K.N., 1972: Light Scattering by Ice Clouds in the Visible and Infrared: A Theoretical Study, J. Atmos. Sci., 29, 524.
- Smagorinsky, J., 1969: "Problems and Promises of Deterministic Extended Range Forecasting", Bull. Amer. Meteorol. Soc., 50, 286-311.
- Smith, W.L. and H.M. Woolf, 1976: "The Use of Eigenvectors of Statistical Covariance Matrices for Interpreting Satellite Sounding Radiometer Observations", J. Atmos. Sci., 33, 1127-1140.
- Sze, N.D., 1976: "Variational Methods in Radiative Transfer Problems", J. Quant. Spect. and Rad. Trans., 16, 763.
- Tracton, M.S. and R.D. McPherson, 1977: On the Impact of Radiometric Sounding Data upon Operational Numerical Weather Prediction at NMC. National Weather Service Office Note 136, 11 pp.
- van de Hulst, H.C., 1968: Asymptotic Fitting, a Method for Solving Anisotropic Transfer Problems in Thick Layers, J. Comp. Phys., 3, 291.
- Weichel, R.L., 1976: Combined Microwave-Infrared Sounding Studies, AFCL-TR-75-0572, Air Force Cambridge Research Laboratory.